

# TGS1 impacts snRNA 3'-end processing, ameliorates survival motor neuron-dependent neurological phenotypes *in vivo* and prevents neurodegeneration

Lu Chen<sup>1,2,3,4,\*</sup>, Caitlin M. Roake<sup>2,3,†</sup>, Paolo Maccallini<sup>5</sup>, Francesca Bavasso<sup>5</sup>, Roozbeh Dehghannasiri<sup>3,6</sup>, Pamela Santonicola<sup>7</sup>, Natalia Mendoza-Ferreira<sup>8</sup>, Livia Scatolini<sup>5</sup>, Ludovico Rizzuti<sup>5</sup>, Alessandro Esposito<sup>9</sup>, Ivan Gallotta<sup>9</sup>, Sofia Francia<sup>10,11</sup>, Stefano Cacchione<sup>5</sup>, Alessandra Galati<sup>5</sup>, Valeria Palumbo<sup>5</sup>, Marie A. Kobin<sup>4</sup>, Gian Gaetano Tartaglia<sup>5,12,13</sup>, Alessio Colantoni<sup>5,12,13</sup>, Gabriele Proietti<sup>12,13</sup>, Yunming Wu<sup>14</sup>, Matthias Hammerschmidt<sup>15</sup>, Cristiano De Pittà<sup>16</sup>, Gabriele Sales<sup>16</sup>, Julia Salzman<sup>3,6</sup>, Livio Pellizzoni<sup>17,18,19</sup>, Brunhilde Wirth<sup>8,20</sup>, Elia Di Schiavi<sup>7,9</sup>, Maurizio Gatti<sup>5,21</sup>, Steven E. Artandi<sup>2,3,\*</sup> and Grazia D. Raffa<sup>5,\*</sup>

<sup>1</sup>Stanford Cancer Institute, Stanford University School of Medicine, Stanford, CA 94305, USA, <sup>2</sup>Department of Medicine, Stanford University School of Medicine, Stanford, CA 94305, USA, <sup>3</sup>Department of Biochemistry, Stanford University School of Medicine, Stanford, CA 94305, USA, <sup>4</sup>Cancer Signaling and Epigenetics Program and Cancer Epigenetics Institute, Institute for Cancer Research, Fox Chase Cancer Center, Philadelphia, PA 19111, USA, <sup>5</sup>Dipartimento di Biologia e Biotecnologie, Sapienza University of Rome, Rome, Italy, <sup>6</sup>Department of Biomedical Data Science, Stanford University, Stanford, CA 94305, USA, <sup>7</sup>Institute of Biosciences and BioResources, IBBR, CNR, Naples, Italy, <sup>8</sup>Institute of Human Genetics, Center for Molecular Medicine Cologne, Institute for Genetics, University of Cologne, 50931 Cologne, Germany, <sup>9</sup>Institute of Genetics and Biophysics, IGB-ABT, CNR, Naples, Italy, <sup>10</sup>IFOM-The FIRC Institute of Molecular Oncology, Milan, Italy, <sup>11</sup>Istituto di Genetica Molecolare, CNR-Consiglio Nazionale delle Ricerche, Pavia, Italy, <sup>12</sup>Center for Life Nano- & Neuro-Science, Fondazione Istituto Italiano di Tecnologia (IIT), Rome 00161, Italy, <sup>13</sup>Center for Human Technology, Fondazione Istituto Italiano di Tecnologia (IIT), Genoa 16152, Italy, <sup>14</sup>Department of Biology, Howard Hughes Medical Institute, Stanford University, Stanford, CA 94305, USA, <sup>15</sup>Institute for Zoology, Developmental Biology, University of Cologne, 50674 Cologne, Germany, <sup>16</sup>Department of Biology, University of Padova, Padua, Italy, <sup>17</sup>Center for Motor Neuron Biology and Disease, Columbia University, NY 10032, USA, <sup>18</sup>Department of Pathology and Cell Biology, Columbia University, NY 10032, USA, <sup>19</sup>Department of Neurology, Columbia University, NY 10032, USA, <sup>20</sup>Center for Rare Diseases, University Hospital of Cologne, University of Cologne, 50931 Cologne, Germany and <sup>21</sup>Istituto di Biologia e Patologia Molecolari (IBPM) del CNR, Rome, Italy

Received June 29, 2022; Editorial Decision July 10, 2022; Accepted July 21, 2022

## ABSTRACT

Trimethylguanosine synthase 1 (TGS1) is a highly conserved enzyme that converts the 5'-monomethylguanosine cap of small nuclear RNAs (snRNAs) to a trimethylguanosine cap. Here, we show that loss of TGS1 in *Caenorhabditis elegans*, *Drosophila melanogaster* and *Danio rerio* results in neurological phenotypes similar to those caused by

survival motor neuron (SMN) deficiency. Importantly, expression of human TGS1 ameliorates the SMN-dependent neurological phenotypes in both flies and worms, revealing that TGS1 can partly counteract the effects of SMN deficiency. TGS1 loss in HeLa cells leads to the accumulation of immature U2 and U4atac snRNAs with long 3' tails that are often uridylated. snRNAs with defective 3' terminations also

\*To whom correspondence should be addressed. Email: [graziadaniela.raffa@uniroma1.it](mailto:graziadaniela.raffa@uniroma1.it)  
Correspondence may also be addressed to Lu Chen. Email: [Lu.Chen@fccc.edu](mailto:Lu.Chen@fccc.edu)  
Correspondence may also be addressed to Steven E. Artandi. Email: [sartandi@stanford.edu](mailto:sartandi@stanford.edu)

†These authors contributed equally.

‡Lead contact.

**accumulate in *Drosophila Tgs1* mutants. Consistent with defective snRNA maturation, *TGS1* and *SMN* mutant cells also exhibit partially overlapping transcriptome alterations that include aberrantly spliced and readthrough transcripts. Together, these results identify a neuroprotective function for *TGS1* and reinforce the view that defective snRNA maturation affects neuronal viability and function.**

## INTRODUCTION

The correct processing of small non-coding RNAs is essential to prevent severe neurodegenerative conditions (1). Small nuclear RNAs (snRNAs) are components of the spliceosomal small nuclear ribonuclear proteins (snRNPs). Defects in the snRNP assembly pathway have been observed in spinal muscular atrophy (SMA), a neurological disease caused by deficiency of the survival motor neuron (SMN) protein (2). Another neurodegenerative disorder, Pontocerebellar hypoplasia type 7 (PCH7), is caused by mutations in the TOE1 deadenylase (Target Of EGR1) that prevents accumulation of 3'-end-extended pre-snRNAs (3).

The Sm class snRNAs include components of both the major (U1, U2, U4 and U5) and minor (U11, U12, U4atac and U5) spliceosome. These snRNAs are transcribed by RNA polymerase II (Pol II) and the formation of their 3' ends is co-transcriptionally controlled (4,5). Nascent U1 and U2 snRNA transcripts are subject to cleavage by the Integrator complex, resulting in precursors carrying extended 3' ends that are trimmed after export to the cytoplasm (6–8).

All snRNAs transcribed by Pol II acquire an m<sup>7</sup>-monomethylguanosine cap (m<sup>7</sup>G/MMG cap) at their 5' end. Immediately after transcription, the monomethylated snRNA precursors bind the cap-binding complex (CBC) and are exported to the cytoplasm (9,10), where they bind the Gemin5 subunit of the SMN complex (11) that mediates their assembly with the seven Sm proteins (Sm core) to form snRNPs (12). The snRNA precursors associated with Gemin5 have extended 3' tails that can be oligoadenylated or uridylated (11). The U2 snRNA precursors have 3' extended tails including 12 genomic-encoded nucleotides, which are trimmed by the TOE1 deadenylase (3).

Following interaction with SMN and the Sm core, the MMG cap of snRNAs is converted to a 2,2,7-trimethylguanosine cap (henceforth abbreviated to TMG cap) by trimethylguanosine synthase 1 (*TGS1*) (13), which physically interacts with SmB and SMN (14). Re-entry of the snRNPs into the nucleus is mediated by both the TMG cap and the Sm core (15,16). In somatic cells of *Xenopus* and mammals, the Sm signal is both necessary and sufficient for nuclear import, while the TMG cap accelerates the rate of import (17–19). Once in the nucleus, the snRNPs concentrate in the Cajal bodies (CBs) and undergo further maturation steps (20).

3'-end processing of snRNAs is thought to occur after TMG cap formation (21), but whether *TGS1* and cap hypermethylation have roles in subsequent steps of snRNP processing is unknown. This is a relevant biomedical issue, as abnormal accumulations of 3'-end-extended snRNA precursors have been observed in PCH7 patients (3) and in

cells deficient for SMN (11). To elucidate the role of *TGS1* in snRNA maturation and its functional relationships with *SMN*, here we explored the phenotypic consequences of *TGS1* loss in human cells and in the *Drosophila*, *Caenorhabditis elegans* and *Danio rerio* model organisms. Collectively, our results indicate that *TGS1* plays a conserved role in 3' processing of snRNAs and acts as a neuroprotective factor that can counteract the phenotypic consequences of SMN deficiency.

## MATERIALS AND METHODS

### *Caenorhabditis elegans* strains

Nematodes were grown and handled following standard procedures, under uncrowded conditions, at 20°C, on NGM (Nematode Growth Medium) agar plates seeded with *Escherichia coli* strain OP50 (22). Wild-type animals used in this work were *C. elegans* variety Bristol, strain N2. The transgenic strains used in this work were: NA1330 *gbIs4* [GBF109 *punc-25::cesmn-1(RNAi)* (200 ng/μl); GB301 *pchs-2::GFP* (10 ng/μl)] III; NA1617 *gbEx593* [GBF109 *punc-25::cesmn-1(RNAi)* (10 ng/μl); GB301 *pchs-2::GFP* (10 ng/μl)]; NA1541 *gbEx568* [GBF321 *punc-25::cekal-1(RNAi)* (10 ng/μl); GB301 *pchs-2::GFP* (10 ng/μl)]; NA1252 *gbEx504* [GBF322 *punc-119::dsRED* (20 ng/μl); *pelt-2::RFP* (30 ng/μl)] (23); and EG1285 *oxIs12* [*punc-47::GFP*; *lin-15(+)*]. EG2185 and N2 were provided by the *Caenorhabditis* Genetics Center (CGC), funded by the NIH Office of Research Infrastructure Programs (P40 OD010440); *Is[punc-47::RFP]* was kindly provided by K. Shen (Stanford University, USA). A complete description of the transgenes obtained in this work is reported in Table 1.

### Transgenic *C. elegans* strains

The constructs GBF329 (*pcetgs-1a::GFP*) and GBF330 (*pcetgs-1b::GFP*) for analyzing the expression of *cetgs-1* isoforms were created by polymerase chain reaction (PCR) fusion (24) of two DNA fragments: the presumptive promoters of *cetgs-1* and the green fluorescent protein (GFP) sequence. The two promoters of *cetgs-1* isoforms (*a* and *b*) have been chosen upstream of the ATG of the two isoforms, to span 360 bp (*cetgs-1a*) and 960 bp (*cetgs-1b*), respectively. The putative regulatory regions were amplified by PCR using as template wild-type genomic DNA. The GFP, followed by the 3'-untranslated region (UTR) of the *unc-54* gene, was amplified from plasmid pPD95.75, kindly provided by A. Fire (Stanford University, CA, USA). The rescue plasmids (GB335 *punc-119::hTGS1* and GB338 *punc-119::cetgs-1*) for pan-neuronal expression were created by cloning the *hTGS1* or *cetgs-1* coding sequence (CDS) into the plasmid pBY103, kindly provided by O. Hobert (Columbia University, NY, USA), which contains the pan-neuronal promoter *punc-119*. *hTGS1* and *cetgs-1* CDS were amplified by PCR from cDNA libraries and cloned in the BamHI site of pBY103. D-type motor neuron (MN)-specific RNA interference (RNAi) transgenic lines were obtained as previously described (23,25). To obtain the specific knock-down of *cetgs-1*, we used a short form of the *unc-25/GAD* promoter (180 bp), which is specifically

**Table 1.** List of the *C. elegans* transgenes

Strain	Transgene name	Transgene description	Notes
NA1539	<i>gbEx579</i>		<i>cetgs-1</i> knock-down in D-type MNs
NA1972	<i>gbEx647</i>	GB335 <i>punc-119::hTGS1</i> (20 ng/ $\mu$ l); <i>podr-1::RFP</i> (30 ng/ $\mu$ l)	<i>hTGS1</i> overexpression in all neurons
NA1981	<i>gbEx648</i>	GB338 <i>punc-119::cetgs-1</i> (20 ng/ $\mu$ l); <i>podr-1::RFP</i> (30 ng/ $\mu$ l); <i>gbls4 III</i>	<i>ceTGS-1</i> overexpression in all neurons with <i>smn-1</i> knock-down in D-type MNs
NA1533	<i>gbEx576</i>	GBF329 <i>pzetgs-1a::GFP</i> (50 ng/ $\mu$ l)	GFP expression under <i>cetgs-1</i> isoform <i>a</i> promoter
NA1535	<i>gbEx577</i>	GBF330 <i>pzetgs-1b::GFP</i> (50 ng/ $\mu$ l)	GFP expression under <i>cetgs-1</i> isoform <i>b</i> promoter

expressed from embryonic to adult stages only in the 19 D-type MNs in the ventral cord and not in other GABAergic neurons (RME, AVL, DVB and RIS) (23,26). For gene silencing, we amplified, from genomic DNA, the same exon-rich region that was used for the RNAi plasmid library prepared for RNAi by feeding experiments (27). Exon-rich regions were amplified in two separate PCRs to obtain the sense and antisense fragments. The *unc-25* promoter was amplified using specific primers. The promoter was subsequently fused to each orientation of the target gene by PCR fusion using internal primers. All primers are available upon request. Germline transformation was accomplished as described (28) by injecting into the gonad of adult animals a DNA mixture containing a transgenic construct together with a phenotypic marker for selection of transgenic progeny. As co-injection marker we used *podr-1::RFP* kindly provided by C. Bargmann, The Rockefeller University, NY, USA [red fluorescent protein (RFP) expression in AWC and AWB neurons] at 30 ng/ $\mu$ l and GB301 *pchs-2::GFP* (GFP expression in the glandular pharyngeal g1 and g2 cells, and in m3 and m4 myoepithelial cells) (29) at 10 ng/ $\mu$ l. At least two independent transgenic lines were examined for each experiment. Genetic crosses were made to transfer transgenes to the appropriate genetic background. In all cases, the presence of the desired transgenes was verified by phenotyping. Two independent clones with the same genotype were examined after each cross, and the mean of the two clones has been reported in the Results. The *punc-25* promoter, used for neuron-specific silencing of *cetgs-1* and *cesmn-1*, is expressed in 19 neurons among a total of 959 somatic cells and ~2000 germ cells in each animal (30), so it is estimated that only 0.6% of total cells have been silenced for *cetgs-1* and *cesmn-1* in each animal (23). Thus, changes in gene expression compared with the wild type cannot be appreciated in whole animals. In contrast, *cetgs-1* overexpression is driven in all 302 neurons thanks to the pan-neuronal promoter *punc-119* and through the formation of extrachromosomal arrays, which carry a variable number of copies (between 80 and 300 of the gene of interest (31).

### *Caenorhabditis elegans* behavioral assay

Well-fed, young adult animals were used for backward movement assay (32) to test D-type MN function. The assay was performed blind on NGM plates, 6 cm in diameter, seeded with bacteria. Using an eyelash, the animal was touched first on the tail to induce a forward movement and then on the head to test for backward movement. A defective movement was scored when animals were unable to fully move backward. For each dataset, the percentage of animals with normal locomotion among the total number

of tested animals was calculated. One-way analysis of variance (ANOVA) test was used for statistical analysis.

### *Caenorhabditis elegans* microscopy analysis

Animals were immobilized in 0.01% tetramisole hydrochloride (Sigma-Aldrich) on 4% agar pads and visualized using Zeiss Axioskop or Leica DM6B microscopes. All microscopes were equipped with epifluorescence and differential interference contrast (DIC) Nomarski optics, and images were collected with Leica Hamamatsu C11440 digital cameras. Confocal images have been collected using a DMi8 confocal microscope.

### Zebrafish experiments

Zebrafish procedures were approved by the local animal protection committee LANUV NRW; reference 84-02.04.2012.A251. Experiments for caudal primary MN (CaP-MN) analysis were performed in the wild-type TL/EK (*Tupfel long fin/Ekkwill*) line.

### Zebrafish injection

Control (non-targeting) and *tgs1* morpholino oligonucleotides (MOs) were purchased from (GeneTools, LLC) using the *tgs1* XM.003197865.5 sequence as reference. MO sequences are reported in Supplementary Table S11. For TGS1 mRNA injection, human *TGS1* cDNA (NM.001317902) was cloned into an N-terminal flag-pCS2 + mRNA expression vector. *In vitro* transcription of 5'-capped mRNAs was performed using the mMACHINE SP6 Transcription Kit (Ambion) following the manufacturer's protocol and as previously described in (33,34). Embryos from TL/EK wild-type crossings were used to visualize the CaP-MN phenotype. Embryos were injected with the respective dose of MOs or mRNA in an aqueous solution containing 0.05% PhenolRed and 0.05% Rhodamine-Dextran (Sigma-Aldrich). At 6–7 h after injection, embryos were sorted according to homogeneity of the rhodamine fluorescence signal.

### Semi-quantitative RT-PCR of zebrafish samples

RNA isolation from zebrafish larvae [~34 h post-fertilization (hpf)] was performed following the procedure described in (35). RNA was extracted using the RNeasy kit (Qiagen) and concentrations were determined by the RiboGreen method (Life Technologies). A 600 ng aliquot of RNA was reverse transcribed to cDNA with the Quantitect Reverse Transcription Kit (Qiagen). The



reverse transcription-PCR (RT-PCR) experiments were performed as previously described in (36). Multiplex analyses were optimized at 30 cycles to amplify both spliced and unspliced *tgs1* transcripts. In addition to the multiplex analyses, single analyses were performed in the linear phase (22–26 cycles) to ensure reliable quantitative measurements and normalization against endogenous control (*ef1a*).

We observed a clear dose-dependent increase of unspliced transcripts with increasing morpholino concentration. Primers were designed using Primer-BLAST and purchased from Integrated DNA technologies (IDT). Primers sequences (Drer-*tgs1* and Drer *ef1a*) are reported in Supplementary Table S11. Amplification products from semi-quantitative RT-PCR were gel-purified using the QIAquick gel extraction kit (Qiagen) and Sanger sequenced. Densitometric analyses were performed with ImageLab 5.2.1 (Bio-RAD).

### Immunostaining of zebrafish caudal primary motor neurons

Zebrafish larvae immunostaining was performed as previously described in (33,34). Briefly, ~34 hpf zebrafish were manually dechorionated, fixed in 4% paraformaldehyde in phosphate-buffered saline (PFA-PBS) and permeabilized by proteinase K digestion of whole larvae. To visualize CaP-MNs, fish larvae were blocked in blocking solution [PBS, 0.1% Tween (PBST) + 5% fetal calf serum (FCS), 2% bovine serum albumin (BSA) and 1% dimethylsulfoxide (DMSO)] and incubated overnight at 4°C with mouse  $\alpha$ -Znpl (Synaptotagmin) antibody diluted 1:150 in blocking solution. After five washes of 1 h with washing solution (PBST + 1% FCS + 1% BSA), the secondary mouse  $\alpha$ -AlexaFluor488 antibody was diluted 1:250 in blocking solution and incubated at 4°C overnight. Following five washes of 20 min each, stained fish were stored in 80% glycerol in PBS at 4°C.

For imaging of CaP-MN, fish were laterally embedded in 2% low melting agarose (LMA) microslides under a binocular microscope. Slides were analyzed with the fluorescence microscope AxioImagerM2 (Zeiss). The first 10 motor axons posterior to the yolk sac were considered for quantification. Based on overall appearance, CaP-MN axons were classified as: normal, truncation (shortened axonal projection) or atrophy (absent axonal projection). Based on terminal branching, axons were classified as normal, mild (branching ventral from the midline), medium (2–3 or more branches at ventral or midline) or severe (>3 branches ventral or dorsal from the midline). Brightfield images of zebrafish larvae were acquired with a Leica S8AP0 binocular attached to an AxioCam ERc5s camera (Zeiss).

### Drosophila strains and transgenic constructs

The *UAS-Smn RNAi* construct [P{TRiP.HMC03832}attP40 (*UAS-SmnRNAi*)] and the *nsyb-GAL4* driver were obtained from the Bloomington Stock Center. The deficiency that removes the *Smn* gene (the *Smn*<sup>X7</sup> allele) is a gift from Dr Artavanis-Tsakonas (37). The *UAS-GFP-dTgs1* strain carries the pPGW-*Tgs1* construct, generated by cloning the *dTgs1* CDS into the pPGW destination vector (stock number 1077, Drosophila Genomics Resource Center, supported by NIH grant 2P40OD010949), using Gateway technology (Thermo Fisher Scientific); the *UAS-mst* construct

(*UAS-CTRL*) encoding the Misato protein is ppGW-GFP-Mst (38). The *UAS-hTGS1* construct carrying human *TGS1* carries the full-length human *TGS1* gene cloned into the pUAST-attB vector (39). Transgenic flies were obtained by injecting the constructs into either the *w*<sup>1118</sup> or the *y*<sup>1</sup> *v*<sup>1</sup>; P{*CaryP*}attP40 (2L, 25C6) strains. All embryo injections were carried out by BestGene (Chino Hills, CA, USA). The *dTgs1*<sup>RI</sup> mutant alleles were generated by CRISPR/Cas9 [clustered regularly interspaced short palindromic repeats (CRISPR)/CRISPR-associated peptide 4] genome editing as described in (40). The *dTgs1*<sup>CB0</sup> mutant allele is the P{PTT-GB}moiCB02140 insertion (41,42). The Oregon-R strain was used as a wild-type control. All flies were reared according to standard procedures at 25°C. Lethal mutations were balanced over either *TM6B*, *Hu*, *Tb* or *CyO-TbA*, *Cy*, *Tb* (43). All genetic markers and special chromosomes are described in detail in FlyBase (<http://www.flybase.org>).

### Cell culture, transfections, generation of *TGS1*- and *SMN*-CRISPR HeLa cell lines and transductions

HeLa S3 cells were cultured in Dulbecco's modified Eagle's medium (DMEM) supplemented with 10% fetal bovine serum (FBS) and penicillin-streptomycin at 37°C, in 5% CO<sub>2</sub>. Lipofectamine 2000 (Life Technologies) was used for all cDNA transfection experiments. *TGS1* or *SMN* CRISPR cells were generated by transfection of HeLa cells with pSpCas9-2A-GFP (PX458) plasmid (44) encoding 3 × FLAG Cas9-T2A-GFP and guide RNAs to the *TGS1* locus (*TGS1-1*, AGAGAAACATTTCCGCCACG; *TGS1-2*, TGTCAGAGCGTATCTTCAGC) (45) or the *SMN* locus (*SMN-1*, CACCCCACTTACTATCATGC). GFP-positive cells were single-cell sorted into 96-well plates by fluorescence-activated cell sorting (FACS), and clones carrying mutations affecting *TGS1* expression were screened by immunoblotting using anti-*TGS1* or anti-*SMN* antibody, respectively.

To generate *TGS1* mutant cells stably expressing FLAG-*TGS1* (*TGS1* rescued cells), we transfected 293T cells with the pCDH-CMV-PURO-3 × FLAG-*TGS1* construct (FLAG-*TGS1*) and packaging constructs; 48 h later, viral supernatant was collected and concentrated using Retro-X (Clontech). HeLa *TGS1* mutant clones were transduced in the presence of 5  $\mu$ g/ml polybrene and selected in 2  $\mu$ g/ml puromycin.

For *TGS1* knockdown, UMUC 3 cells (46) were cultured in Eagle's minimum essential medium (EMEM)-Eagle's balanced salt solution (EBSS) supplemented with 2 mM glutamine, 0.1 mM non-essential amino acids, 10% FBS, 1.5 g/l sodium bicarbonate, 1 mM sodium pyruvate, and treated for up to 10 days (every 72 h) with 50 nM SMART-pool: siGENOME *TGS1* siRNA or ON-TARGET plus Non-targeting siRNA using Dharmafect I (Dharmacon). The *PAPD5 KO* and *TCABI KI* cell lines are described in (47) and (48). Cumulative population doubling values were determined over a period of 30 days. A total of 1.5 × 10<sup>4</sup> cells/well were seeded in 6-well plates in duplicates; cells were counted after 72 h.

### Western blotting

For western blotting, 10–50 µg of protein extracts were separated by sodium dodecylsulfate–polyacrylamide gel electrophoresis (SDS–PAGE), transferred onto a polyvinylidene fluoride (PVDF) membrane (GE Healthcare, RPN303F) and blotted according to standard procedures. Milk (5%) in PBST was used for all blocking and antibody incubation steps; PBST was used for all washes. Detection was performed with the SuperSignal™ West Pico Chemiluminescent Substrate (Thermo); images were acquired with Chemidoc (Biorad) and analyzed using the QuantityOne image analysis software (Biorad), or with the Odyssey infrared imaging system (LiCoR). We used the following primary antibodies: FLAG mouse monoclonal (clone M2), Sigma, F1804, 1:1000; PIMT/TGS1, Bethyl A300-814A (lot 1), 1:1500; β-tubulin, mouse monoclonal (clone D-10) Santa Cruz, SC-5274; SMN, mouse monoclonal antibody (clone 2B1), 05-1532 Sigma-Aldrich, 1:1000; Coilin, mouse monoclonal [IH10], abcam, (ab87913); CBP20, rabbit NCBP2, Bethyl laboratory, A302-553A; and GAPDH, rabbit, CST, D16H11. Primary antibodies were detected with horseradish peroxidase (HRP)-conjugated anti-mouse or anti-rabbit 1:5000 (GE Health Care).

### Immunofluorescence staining

Immunofluorescence experiments were carried out on cells grown on coverslips. Cells were fixed with 4% PFA and permeabilized with 0.5% Triton X-100 in PBS. Coverslips were incubated with primary antibodies in 3% BSA for 1 h at room temperature: monoclonal anti-SMN (05-1532 Sigma-Aldrich clone 2B1, 1:1000); rabbit anti-Coilin (H300 Santa Cruz SC-32860, 200 µg/ml); rabbit anti-TCAB1 ((49), 25 ng/ml). Coverslips were washed three times with PBS and incubated with secondary Alexa Fluor-conjugated antibodies (Jackson ImmunoResearch). Coverslips were washed three times in PBS, counterstained in a 300 nM 4',6-diamidino-2-phenylindole (DAPI) solution and mounted in ProLong Gold Anti-fade Mountant. Images were captured on a Leica wide-field fluorescence microscope and processed using Leica LAS AF and Photoshop.

### RNA immunoprecipitation (RIP) of TMG-capped RNA

TRIZol-purified RNA was treated with DNase and subjected to immunoprecipitation with the R1131 anti-TMG cap-specific antibody (50). A 50 µl aliquot of protein G beads was washed with PBS and blocked with 20 µg of tRNA and 20 µg of BSA, then washed with NT2 buffer [50 mM Tris–HCl pH 7.5; 150 mM NaCl; 1 mM MgCl<sub>2</sub>; 0.05% Nonidet P40 (NP40); 1 mM dithiothreitol (DTT); 100 U/ml RNasin; 400 µM vanadyl ribonucleoside complexes (VRCs)] and coupled overnight to either 20 µl of anti-TMG cap antibody or 1 µg of IgG in 250 µl of NT2 buffer. Beads were then briefly washed with NT2 buffer and incubated with TRIZol-purified RNA in 250 µl of NT2 buffer for 2 h at 4°C, while rotating. Beads were then washed six times for 2 min while rotating with NT2 buffer, and precipitated RNA was TRIZol extracted. Both TMG-immunopurified and input RNAs were then subjected to

reverse transcription and real-time quantitative PCR (RT-qPCR; see below).

### Purification of yeast U1 and U2 snRNAs as spike-in controls for TMG-IPs

To extract total yeast RNA, 1 ml of suspension culture of *Saccharomyces cerevisiae* (YPD base + 1% glucose) was pelleted and resuspended in 500 µl of TRIzol, together with 100 µl of TRIzol-pre-washed glass beads (425–600 µm, Sigma G-8772). The mixture was shaken vigorously for at least 15 min on a vortexer to ensure efficient lysis and thereby optimal yield. RNA was extracted with Direct-Zol (Zymo R2050) including the DNase step, eluted in ddH<sub>2</sub>O, snap-frozen and stored at –80°C. Direct-Zol was performed according to the instructions except that an extra 2 min top speed centrifugation was added to get rid of residuals from the column before the elution step.

To prepare RNA molecular weight marker for yeast U1 (SNR19, 568 nt) or yeast U2 (LSR1, 1175 nt), 20 µl *in vitro* transcription (IVT) reactions were carried out (HiScribe T7 kit, NEB E2040). IVT DNA templates were generated by PCRs, in which two randomly selected amplicons of 568 or 1175 nt were amplified from the vector px458 (Addgene #48138) using forward primers that begin with the T7 promoter sequence 5'-AATACGACTCACTATAG-3'. The IVT-RNA markers were purified by Direct-Zol.

For gel purification of yeast U1 and U2, 10 µg of total yeast RNA was resolved in a 3.5% urea–PAGE gel (Hoefer Vertical Unit) and stained with SYBR Green II dye (Sigma, S9305, used at 1:10 000). RNA species co-migrating with IVT RNA markers (568 nt for yeast U1 and 1175 nt for yeast U2) were excised and eluted from the gel according to (51) in Gel Elution buffer (20 mM Tris–HCl pH 7.5, 250 mM sodium acetate, 1 mM EDTA, 0.25% SDS) with end-to-end mixing overnight. Gel eluates were finally purified by Direct-Zol. The presence and enrichment for yeast U1 or yeast U2 from the corresponding gel slices were confirmed by RT-qPCR.

### TMG immunoprecipitation (TMG-IP) from whole-cell extracts

HeLa cells cultured in a 15 cm dish were trypsinized, washed with PBS and resuspended in RBS-250 buffer [250 mM NaCl, 10 mM Tris–HCl pH 7.4, 2.5 mM MgCl<sub>2</sub>, 0.1% NP40, with freshly added protease inhibitors (Sigma P8340) and RNase inhibitor (Lucigen 302812) as 1000× stock]. Cells were lysed with a water bath sonicator (Q-Sonica Q800) with 70% energy output three times for 30 s each. Cell lysates were clarified by centrifugation at 13 000 × g at 4°C for 20 min. The supernatant was quantitated by Bradford protein assay (BioRad 5000006) before snap-freezing, and stored at –80°C. Yeast purified U1/U2 snRNAs were spiked into 200 µg of whole-cell RSB extracts, with 10% of such input set aside and stored at 4°C. Protein A–Sepharose beads (Invitrogen 101041) were pre-washed by PBS and blocked in PBS/1% BSA (w/v) solution (Jackson ImmunoResearch 001-000-162). For each immunoprecipitation, a 10 µl bed volume of beads or 20 µl of slurry were coupled with 4 µg of anti-TMG antibodies (EMD Millipore, MABE302, clone

K121) or control IgGs for 2 h and then combined with the input extract for 2 h rotation at 4°C. The immunoprecipitated complex was then washed and eluted with TRIzol, in parallel with the 'Input', followed by the Direct-Zol procedure including the DNase I step and subjected to reverse transcription and RT-qPCR (see below).

### RT-qPCR

Total RNA was extracted with TRIzol reagent (Ambion), treated with Ambion™ DNase I (RNase-free) and extracted with phenol/chloroform. The integrity of RNA samples was evaluated by gel electrophoresis. A 1 µg aliquot of intact RNA (with a 28S:18S rRNA ratio = 2:1) was reverse transcribed with the RevertAid H Minus Reverse Transcriptase kit (Thermo Scientific, EP0451). Real-time PCRs were performed with the Brilliant II SYBR® Green QPCR Master Mix (Agilent, 600828). The relative quantification in gene expression was carried out using the  $2^{-\Delta\Delta C_t}$  method (52). Using this method, we obtained the fold changes in gene expression normalized to the 5.8S gene (the amplification efficiencies were not significantly different for the target and reference among all samples). A total of three experiments were performed for three biological replicates and the significance was assessed by one- or two-way ANOVA.

For RT-qPCR of RNA immunoprecipitated with the R1131 antibody, samples were processed as above; fold change was calculated by normalizing each RIP sample to the relative input.

In RIP-qPCR analysis, the values reported in the histogram bars represent the fold enrichment of RNA in each immunoprecipitation relative to TMG-IP from control samples (expressed as a percentage of input) and were calculated as follows:

fold enrichment of RNA in the immunoprecipitate, relative to control immunoprecipitate =  $2(-\Delta\Delta C_t [\text{RIPtest sample}/\text{RIPCTR}])$ , where

$$\Delta\Delta C_t [\text{RIPtest sample}/\text{RIPCTR}] = \Delta C_t [\text{RIP}]_{\text{test sample}} - \Delta C_t [\text{RIP}]_{\text{CTR}}$$

and

$$\Delta C_t [\text{RIP}]_{\text{test sample}} = \left( \frac{C_t [\text{IP}]_{\text{test sample}} - C_t [\text{Input}]}{\text{test sample} - \log_2(\text{Input}/\text{IP dilution factor})} \right)$$

For RT-qPCR of RNA immunoprecipitated with the K121 antibody, the RNA eluates were quantitated by one-step RNA-to-Ct qRT-PCR (Brilliant III SYBR green mix, Agilent 600886) containing MMLV reverse transcriptase and ROX reference dye. Reactions (5 µl) were performed in duplicate in a 384-well plate, using the QuantStudio 6 Pro qPCR system (Applied Biosystems).

The Ct or Cq value for each RNA target in TMG-IPs was normalized to the corresponding Inputs using the  $2^{-\Delta C_t}$  method. These '% of input' values of human RNA targets were then normalized with those of yeast U1 or yeast U2 (the spike-in controls), enabling direct comparison across TMG-IPs from different extracts. Three independent experiments were performed, and the resulting data were analyzed and graphed with Prism software. For *C. elegans* ex-

periments, worm pellets were flash-frozen three times before RNA extraction in TRI Reagent® (Merck, Darmstadt, Germany), according to the manufacturer's protocol. RNA was treated with DNA-free™ DNA Removal (Invitrogen™). Reverse transcription was performed with SuperScript Reverse Transcriptase (Invitrogen™) and real-time PCRs were performed using the Power SYBR Green PCR Master Mix (Applied Biosystems) on the 7900HT Fast Real Time PCR System (Applied Biosystems), following standard procedures. *cetgs-1* expression levels were normalized to the average level of the housekeeping gene *ceact-1*. Each experimental assay was performed in triplicate in three independent experiments. Primers are listed in Supplementary Table S11.

### Cell fractionation and northern blotting

Nuclear extracts (NE) and cytosolic extracts (S100) were obtained using the Dignam protocol as shown in (53). For northern blotting, total RNA is extracted by resuspending pelleted cells with TRIzol reagent. Nuclear and cytoplasmic RNAs were extracted from 4 µg of NE and 12 µg of S100, respectively with a 5× volume of TRIzol. Precipitated RNAs were dried and resuspended sequentially in 5 µl of ddH<sub>2</sub>O, and then with 5 µl of RNA loading dye, containing 0.1× TBE, 50 mM EDTA, 0.1% bromophenol blue, 0.1% xylene cyanol, 93% formamide. Boiled and rapidly chilled RNAs were fractionated in a 18 × 24 cm 6% urea-PAGE (19:1) gel, running at 45 V for > 20 h until the bromophenol blue run-off. The gel was then transferred to a Hybond-N nitrocellulose membrane under 400 mA for 2 h in the cold room. The post-transfer gel was stained by ethidium bromide (EtBr) for rRNAs as loading control. UV-cross-linked membrane was blocked and hybridized in ULTRAhyb, in a 42°C oven overnight, with <sup>32</sup>P-end-labeled oligonucleotide probes (sequence listed in Supplementary Table S11). The washed membrane was exposed to a phosphor-imager screen, scanned by a Typhoon scanner and quantitated with the TotalLab software.

### Single molecule FISH (Yn *situ*)

The single molecule fluorescence *in situ* hybridization (FISH) protocol was carried out according to the protocol described in (54). Oligonucleotides used as Yn *situ* probes for U1 and U2 snRNAs are listed in Supplementary Table S11.

### Nascent RNAend-Seq and steady-state 3' RACE-Seq

For the isolation of nascent RNA from HeLa cells, cells were pulsed for 1 h with 250 µM 4-thiouridine (4sU) or for 4 h with 50 µM 4sU. For chase experiments, 4sU was removed, the cells were washed in PBS and 2.5 mM uridine-containing medium was added. Cells were harvested and cell pellets resuspended in TRIzol. RNA was extracted using the standard TRIzol protocol. A 100 µg aliquot of RNA was biotinylated with Biotin-HPDP (Pierce 21341) at 0.5 mg/ml in 40% demethylformamide (DMF) and 10 mM Tris pH 7.4, 1 mM EDTA, for 1.5 h at room temperature. *In vitro* transcribed luciferase RNA transcribed



in the presence of 4sU was spiked into the biotinylation mixture for a final concentration of 0.01 ng/ $\mu$ l. RNA was extracted using isopropanol/ethanol precipitation. Biotinylated RNA was immunoprecipitated from total RNA using the mMac5 Streptavidin Kit (Miltenyi 130-074-101). The depleted fraction was recovered using isopropanol/ethanol precipitation. Biotinylated RNA was released from beads using 100 mM DTT and cleaned using an RNeasy MinElute Kit (QIAGEN 74204). Half of the eluted RNA or 600 ng of depleted RNA was ligated to 5  $\mu$ M of 5' adenylated, 3' blocked adaptor (Universal miRNA cloning linker, NEB S1315S) with 250 U of T4 RNA ligase-truncated KQ (NEB M0373S), 25% polyethylene glycol (PEG) 8000, and 1  $\mu$ l of RnaseOUT (ThermoFisher 10777019) in a 20  $\mu$ l reaction at 25°C for 16 h. Ligated RNA was cleaned up with RNA clean and concentrator columns (Clontech 740955.50) and DNase treatment. cDNA was synthesized with universal primer and SuperScript III (ThermoFisher 18080093). Amplification was carried out with Phusion (New England Biosystems M0530) and primer sets universal/specific for the RNA of interest. PCR products were directly run on an 8% PAGE gel and visualized with SYBR Gold (ThermoFisher S-11494), or subject to AMPure XP beads (Beckman Coulter A63881) for PCR clean-up and library preparation. Libraries were prepped using a Kapa Hyperprep Kit (Kapa KK8504), quantified with Qubit and Bioanalyzer, and run on Illumina miSeq at the Stanford Functional Genomics Facility. Reads were paired using the fastq-join tool at Galaxy (<http://usegalaxy.org>). Reads were binned into the various forms of each specific snRNA using custom Python scripts ([https://github.com/cmroake/NAR\\_TGS1](https://github.com/cmroake/NAR_TGS1)), and the number of reads in each bin was normalized to total snRNA reads. Primer sequences can be found in Supplementary Table S11. Data have been deposited at SRA with BioProject ID PRJNA628085.

### Transcriptome library preparation and RNA-sequencing

Total RNA was extracted with TRIzol reagent (Ambion), treated with Ambion™ DNase I (RNase-free) and extracted with phenol/chloroform. RNA samples were quantified and quality-tested by Agilent 2100 Bioanalyzer RNA assay (Agilent Technologies, Santa Clara, CA, USA). The TruSeq Stranded mRNA kit (Illumina, San Diego, CA, USA) was used for library preparation following the manufacturer's instructions (library type: fr-firststrand). Final libraries were checked with both Qubit 2.0 Fluorometer (Invitrogen, Carlsbad, CA, USA) and Agilent Bioanalyzer DNA assay. Libraries were then prepared for sequencing and sequenced on paired-end 150 bp mode on NovaSeq 6000 (Illumina, San Diego, CA, USA).

The number of reads (in millions) produced for each sample is listed in Table 2.

Primary bioinformatic analysis includes the following steps.

Basecalling and demultiplexing. Processing raw data for both format conversion and demultiplexing by Bcl2Fastq 2.20 version of the Illumina pipeline ([https://support.illumina.com/content/dam/illumina/support/documents/documentation/software\\_documentation/bcl2fastq/bcl2fastq2-v2-20-software-guide15051736-03.pdf](https://support.illumina.com/content/dam/illumina/support/documents/documentation/software_documentation/bcl2fastq/bcl2fastq2-v2-20-software-guide15051736-03.pdf)).

**Table 2.** Number of Illumina sequencing reads

Sample name	Reads (M)
ID1232.1-1A-CTR1	311.29
ID1232.2-1B-CTR2	310.44
ID1232.3-2A-TGS1 M1	299.96
ID1232.4-3A-TGS1 M2	314.74
ID1232.5-4A-SMN C1	358.39
ID1232.6-5A-SMN C2	272.79

Adapter masking. Adapter sequences are masked with Cutadapt v1.11 from raw fastq data using the following parameters: `-anywhere` (on both adapter sequences) `-overlap 5` `-times 2` `-minimum-length 35` `-mask-adapter` (<http://dx.doi.org/10.14806/ej.17.1.200>).

Folder 'raw\_reads' contains files with raw reads (R1, first read sequence; R2, second read sequence) and a multiqc\_report.html file, which aggregates results from primary bioinformatic analysis into a single report file with parameters that give insight into overall processing and sequencing quality.

### Transcript reconstruction and analysis

Paired-end Illumina sequencing was performed on RNA isolated from TGS1 mutant clones (M1 and M2), SMN mutant clones (C1 and C2) and parental HeLa cells (CTRL, two replicates) at a depth of 160 million reads/sample. Mutant samples were clustered based on both transcript and gene expression profiles (Supplementary Figure S7). We mapped reads to the human reference genome (Gencode annotation v33) using STAR v2.7.1a (55) and ran Scallop (56) on the resulting BAM files to find all novel transcripts in the data. We combined the Scallop-detected novel transcripts with the reference transcripts and used Kallisto (57) to quantify transcript expression levels. Differentially expressed novel and annotated transcripts were found using Sleuth v0.30.0 (57) (Wald test, false discovery rate-adjusted  $P$ -value  $< 0.05$ , beta value  $> 2$ ). We compared the 3' side of each novel transcript with its closest annotated transcript to determine whether the novel transcript has a shorter, extended or the same 3' side as compared with the annotated transcript. To investigate the extent of global splicing changes induced by TGS1 and SMN knockouts, we performed differential splicing analysis. We extracted alternative splicing events from the GTF file containing all novel and annotated transcripts and then used SUPPA2 (58) to find significantly changed alternative splicing events. We considered all seven major categories of alternative splicing events and found the percentage of splicing inclusion (PSI) for each extracted splicing event. A differentially spliced event between mutant and control samples should have a difference in PSI of at least 0.1 and an adjusted  $P$ -value  $< 0.05$ .

*Methodological approach used for quantification of intron retention (IR) levels (Figure 7D).* We performed a transcriptome-wide analysis of the expression levels for the major transcript isoforms (i.e. the transcript without the intron) in the IR events. IR is quantified by the PSI, which is computed as the percentage of reads mapping to the in-

tron inclusion isoform, relative to total reads mapping to both intron inclusion and intron exclusion isoforms. Differential expression of the spliced isoforms (intron exclusion) was computed as the difference in TPM (or transcript per million) values (dTPM) between mutant and control cells (plotted on the *x*-axis in Figure 7E, F). The expression of the major transcripts in most of the significant IR events does not change considerably (small difference in TPM) between control and mutant samples (Figure 7E, F). As an independent pipeline for detecting differentially expressed transcripts, we also used a combination of Salmon (59) for transcript quantification and DESeq2 for differential analysis. Statistical analyses on individual transcripts were made with the test implemented in the software.

### Nanopore sequencing and analyses

**Data generation.** Total RNA was extracted with TRIzol reagent (Ambion), treated with Ambion™ DNase I (RNase-free) and extracted with phenol/chloroform. All samples have been checked for RIN score > 8 by Agilent 2100 Bioanalyzer RNA assay (Agilent Technologies). The same extracted RNA was used both for Illumina and Nanopore library preparation. Nanopore libraries were generated according to the PCR-cDNA barcoding (SQK-PCB109) protocol and sequenced on FLO-MIN106 flow cells for 48–72 h with –180 mV starting voltage (see Supplementary Figure S9).

**Basecalling and mapping.** Samples were sequenced using Oxford Nanopore MinION on FLO-MIN106 flow cells. Primary data acquisition was performed by MinKNOW. Supplementary Figure S9 reports information about each run. Basecalling and demultiplexing of Fast5 files obtained by sequencing were performed using Guppy v4.2.2. Reads with Qscore > 7 were mapped to the hg38 genome using Minimap2 v2.17 (60) with parameters -ax splice.

**Differential splicing analysis.** To assemble and quantify transcripts from Nanopore reads, we used FLAIR v1.4 (61). BAM files obtained with Minimap2 were converted into BED12 files using the bam2Bed12.py utility included in FLAIR. After this, splice junctions of reads were corrected using the FLAIR correct module employing both the GENCODE v33 GTF file (gencode.v33.chr\_patch\_hapl\_scaff.annotation.gtf) (62) and short Illumina reads of the corresponding samples. BED12 files were then filtered to maintain only reads with at least one splice junction. Filtered BED12 files from all samples were used to assemble the transcriptome using the FLAIR collapse module, providing the GENCODE GTF file to annotate the results and requiring at least 10 supporting reads to identify novel transcripts. Transcripts from both the GENCODE and FLAIR GTF files were quantified using the FLAIR quantify module. The TPM values were thus calculated and provided to SUPPA2 to identify significantly changed splicing events, following the same procedure used for Illumina short reads.

**Analysis of transcript readthrough.** To study readthrough transcription in wild-type and mutant samples, we first as-

signed multi-exonic corrected reads to their corresponding genes starting from the GTF of assembled transcripts obtained by running another run of FLAIR collapse, with the minimum number of supporting reads set to 3 to identify all the possible splicing junctions for each gene. Each read was assigned to the gene with which it shared the highest number of splicing junctions. For the identification of the last exon of each gene, we first retained only those transcripts from the reference GTF that have an average TPM of > 1 in at least one condition (wild type and TGS1 mutant in wild type versus TGS1 comparison, wild type and SMN mutant in wild type versus SMN comparison); then, for each gene, we selected the last exon of the transcript with the most distal termination site. BEDTools v2.29.1 intersect module (63) was employed to select, among the reads assigned to each gene, those mapping to the last exon. Such reads, each one representing a different transcript, were classified as readthrough if their last mapping position was > 10 nt downstream of the termination of the last exon. Differential readthrough analysis was performed by comparing each mutant sample against the pooled WT sample, obtained by combining the reads of both WT samples. For each last exon having at least 10 reads in both WT and mutant samples under analysis, the proportion of readthrough reads in both samples was compared by performing a Fisher's exact test. In this way, we identified differential readthrough events (DREs) as those having a *P*-value < 0.05. DREs in which the proportion of readthrough reads was higher in the mutant sample and those in which such a proportion was higher in the control samples were defined as 'Preferential Readthrough in Mutant' and 'Preferential Readthrough in CTR' events, respectively. The reads mapping to exons undergoing 'Preferential Readthrough in Mutant' events were used to determine the association between readthrough and differential splicing. Readthrough reads from mutant samples were classified as aberrant if their splice junction chains were not found among the non-readthrough reads from the pooled wild-type sample. The same was done for the non-readthrough reads from mutant samples. The proportions of aberrant reads among readthrough and non-readthrough reads were compared using the  $\chi^2$  test. To identify the alternative splicing events carried by aberrant reads, we generated several GTF files, each one containing an aberrant read and the non-readthrough reads from the pooled wild-type sample, and provided such files to the SUPPA2 generateEvents module.

To identify fusion transcripts of adjacent genes, we focused on readthrough reads with one or more exons after the termination site and searched for overlaps with downstream genes, defined as those genes for which the first splicing junction is located after the last splicing junction of the gene to which the readthrough reads were assigned. We also evaluated whether at least one splice junction of the overlapping readthrough reads coincided with a splice junction of the downstream gene.

### Phylogenetic alignment

TGS1 homologs were identified by searching in the UniProt knowledgebase (<https://www.uniprot.org/>). The amino acid



alignment was built using Geneious prime employing Clustal Omega. To build the phylogenetic tree, pairwise distances were calculated based on the multiple sequence alignment using the Jukes–Cantor distance model. The tree was built using the UPGMA method.

## Statistics

Statistical analyses were performed in GraphPad Prism 6. Type of test, sample size, data representation and *P*-values are indicated in the figure legends.  $P \leq 0.0001$  is indicated as \*\*\*\*;  $P > 0.05$  was considered not significant.

## RESULTS

### The *C. elegans* TGS1 ortholog is expressed in motor neurons and required for neuron survival and worm locomotion

To investigate the role of TGS1 in the nervous system and its relationships with SMN biology, we exploited the *C. elegans* model (23). We first analyzed the expression of the *C. elegans* ortholog of TGS1, *T08G11.4* (Supplementary Figure S1) (64), hereafter referred to as *cetgs-1*, using a GFP reporter approach (24) in which the promoter regions of the two annotated *cetgs-1* isoforms were fused to GFP (*pcetgs-1::GFP a* and *b*). Both isoforms are expressed in ventral cord MNs, 19 of which are D-type  $\gamma$ -aminobutyric acid (GABA) motor neurons (MN), which are specifically marked by the expression of *punc-47::RFP* (Figure 1A) (65,66).

To selectively silence *cetgs-1* in the D-type MNs, we generated a strain carrying the *punc-25::cetgs-1(RNAi)* transgene. This strain is viable, fertile and has a normal development. As a control, we used a transgenic RNAi line that targets *cekal-1*, a neurodevelopmental gene not expressed in the D-type MNs (67). We also exploited a *cesmn-1(RNAi)* line expressing an extrachromosomal RNAi construct (23). D-type MNs control *C. elegans* backward movement (68). A total of 86% of wild-type controls and 85% of *cekal-1*-silenced animals showed normal backward locomotion; this proportion was reduced to 40% and 29% in *cetgs-1(RNAi)* and *cesmn-1(RNAi)* worms, respectively (Figure 1B), indicating that both *cetgs-1* and *cesmn-1* are required for proper MN function and locomotor behavior.

We next asked whether the *cetgs-1*-dependent locomotion defect is due to an alteration in MN morphology and survival. We introduced in *cetgs-1(RNAi)* animals the *oxIs12[punc-47::GFP]* transgene that expresses GFP in D-type MNs, allowing their visualization in living animals. Wild-type or *cekal-1*-silenced worms invariably showed 19 D-type MNs, each extending a circumferential commissure to the dorsal side (Figure 1C–E) (68). In *cetgs-1(RNAi)* animals, the number of visible D-type MNs was on average seven per worm, while *cesmn-1(RNAi)* animals displayed only four neurons/worm, as previously reported (23) (Figure 1C, D). The D-type MNs of *cetgs-1(RNAi)* animals ( $n = 606$  commissures) showed a defect in axonal morphology, consisting of extra branching and guidance defects (Figure 1E). This defect was present in 14% of the commissures of *cetgs-1(RNAi)* worms but was never observed in control ( $n = 586$ ) or *cekal-1(RNAi)* ( $n = 410$ ) animals

( $P < 0.0001$ ; non-parametric *z*-test.). Remarkably, a similar defect was found in *cesmn-1* knockdown worms (23).

Next, we expressed in D-type MNs either human TGS1 (*punc-119::hTGS1*, referred to as *hTGS1*) or the RFP *dsRED* that served as a control (*punc-119::dsRED*). *hTGS1*, but not *dsRED*, partially rescued the MN loss caused by *cetgs-1(RNAi)* (from seven to nine neurons/animal; Figure 1C, D), indicating that this phenotype is specifically caused by *cetgs-1* silencing and suggesting that the TGS1 requirement for neuron survival is conserved from worms to humans.

Finally, we asked whether the loss of D-type MNs observed in *cetgs-1(RNAi)* worms is caused by cell death. Apoptotic MN death in *cesmn-1* knocked down animals is revealed by the accumulation of an endogenous auto-fluorescent marker (23). Wild-type worms showed no dying MNs, while *cekal-1(RNAi)* worms showed an average of one dying MN per animal. In contrast, *cetgs-1(RNAi)* and *cesmn-1(RNAi)* worms displayed seven and eight dying MNs per worm, respectively (Figure 1F, G). Thus, loss of either *cesmn-1* or *cetgs-1* causes D-type MN death.

### *cetgs-1* overexpression mitigates the defects elicited by *cesmn-1* depletion

To determine whether *cetgs-1* interacts genetically with *cesmn-1*, we expressed *cetgs-1* under the control of a pan-neuronal promoter (*punc-119::cetgs-1*, referred to as *cetgs-1*) in worms that also express an integrated *cesmn-1* RNAi construct [*cesmn-1(RNAi Is)*] (23). The overexpression of *cetgs-1* was confirmed by RT-qPCR (Figure 1H). A total of 62% of the *cesmn-1(RNAi Is)* worms showed abnormal locomotion. Expression of *cetgs-1* in these worms lowered the proportion of animals with abnormal locomotion to 28% (Figure 1B), while *dsRED* expression did not change the frequency of worms with locomotory defects (68%,  $P = 0.9$ ) (Figure 1B). In addition, while in *cesmn-1(RNAi Is)* or *cesmn-1(RNAi Is); dsRED* worms, we observed an average of nine dying MNs/worm, in the presence of the *cetgs-1* or *hTGS1* transgenes, the average number of dying MNs was slightly but significantly lowered to seven and eight, respectively (Figure 1F, G). Thus, *cetgs-1* overexpression partially suppresses locomotion defects and neuronal death caused by *cesmn-1* silencing.

### Overexpression of dTgs1 ameliorates the Snn loss-of-function phenotype in *Drosophila*

We next assayed the effects of TGS1 overexpression in a fly SMA model. It has been reported that *Drosophila* Tgs1 (dTgs1) depletion affects motor behavior (40,69,70). We have previously shown that RNAi against *Snn* in neurons perturbs the circuits that control post-eclosion events, leading to defective wing expansion (71). A similar phenotype has been observed in hypomorphic *dTgs1* mutants (40). We generated flies expressing a *UAS-Snn RNAi* construct in neurons, using the *nsyb-GAL4* driver. A total of 16% of these *Snn RNAi* flies displayed unexpanded wings (Figure 2A, B), and this percentage was increased to 44% when RNAi was performed in flies carrying only one copy of *Snn+* ( $\Delta Snn/+$ ; Figure 2B). We then examined flies co-expressing *UAS-Snn-RNAi* and *UAS-dTgs1*, both driven

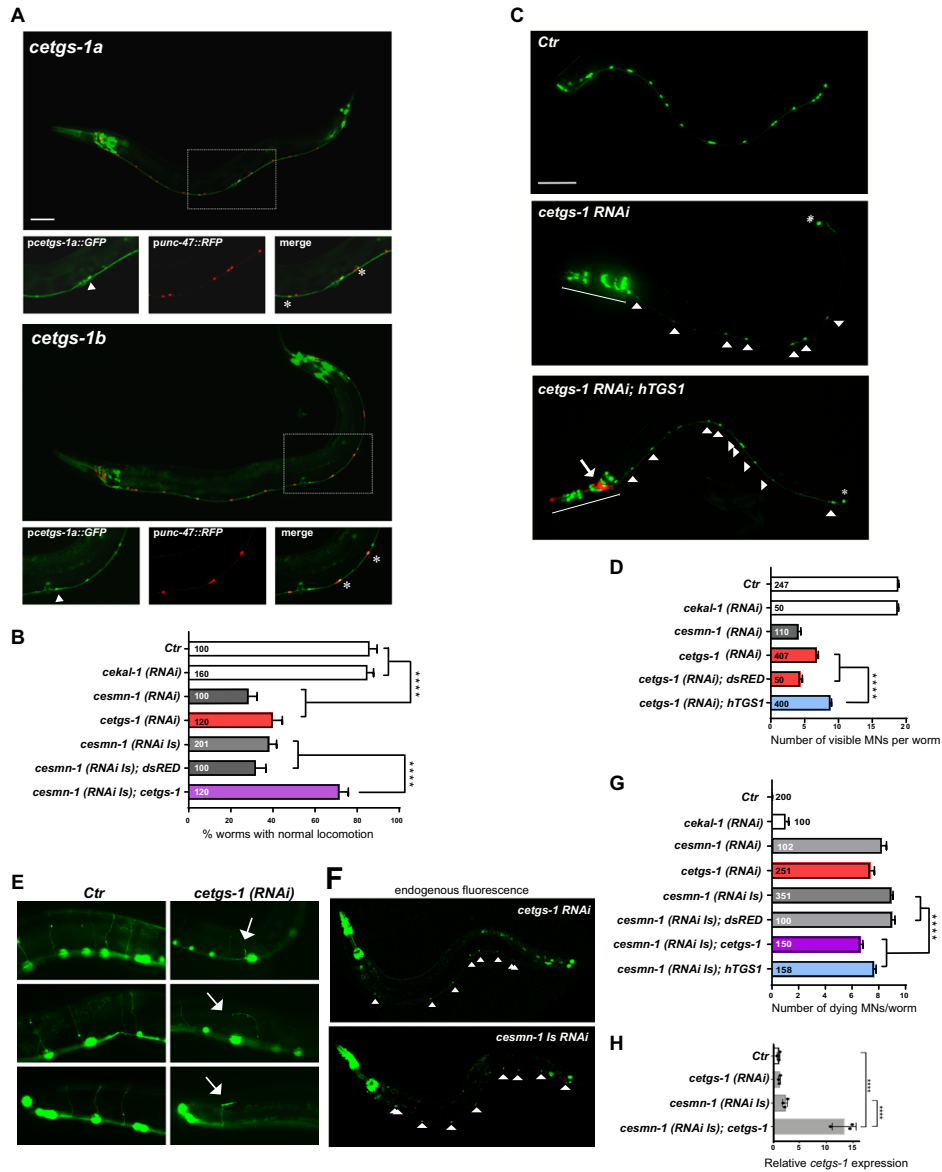


**Figure 1.** Knockdown of *cetgs-1* or *cesmn-1* in D-type MNs results in similar phenotypes that are rescued by *cetgs-1* and *hTGS1* overexpression. (A) The promoters of the *pCetgs-1a* and *pCetgs-1b* isoforms drive the expression of GFP in MNs of the ventral cord. D-type (GABA) MNs express RFP under the control of the MN-specific promoter (*punc-47*). In merged images, the D-type MNs expressing both *cetgs-1* (GFP) and *punc-47* (RFP) are marked by asterisks. The cells expressing only *cetgs-1* (GFP) are MNs other than D-type (arrowheads). Anterior is left and ventral is down in all images. Scale bar, 50  $\mu$ m. (B) Knockdown of *cetgs-1* or *cesmn-1* in D-type MNs leads to similar locomotion defects. Wild-type (Ctrl) and *cekal-1*-silenced animals are controls. The locomotion defect elicited by *cesmn-1* silencing is rescued by *cetgs-1* (driven by the pan-neuronal *punc-119* promoter) but not by *dsRED* expression. Bars represent the percentage of animals with normal backward locomotion  $\pm$  SEM, from at least two independent lines/clones. Numbers within bars are the animals tested. \*\*\*\* $P < 0.0001$  (one-way ANOVA). No statistically significant differences were observed between *cesmn-1 (RNAi)* and *cetgs-1 (RNAi)* ( $P = 0.41$ ) or *cesmn-1 (RNAi)* and *cesmn-1 (RNAi Is)* ( $P = 0.50$ ). (C) Transgenic worms expressing GFP [*oxIs12 (punc-47::GFP)*] show 19 D-type MNs of the ventral cord (Ctrl). *cetgs-1 (RNAi)* worms display fewer GFP-expressing MNs in the ventral cord compared with controls. This phenotype is partially rescued by *hTGS1* expression. MNs are indicated by arrowheads; the RNAi construct is not expressed in the tail, where one GFP-positive cell is always detectable (asterisk); the heads (underlined) express the *pchs-2::GFP* injection marker in both *cetgs-1 (RNAi)* and *cetgs-1 (RNAi); hTGS1* worms; the latter were also injected with the *podr-1::RFP* marker (arrow). Scale bar, 75  $\mu$ m. (D) Quantification of ventral cord D-type MNs. Neuron loss caused by *cetgs-1* knockdown is partially rescued by pan-neuronal expression of human *TGS1 (hTGS1)* but not of *dsRED*. Each bar represents the mean number of visible MNs from at least two independent lines/clones  $\pm$  SEM. Numbers within the bars are the animals tested. \*\*\*\* $P < 0.0001$  (one-way ANOVA). (E) In *oxIs12 [punc-47::GFP]* transgenic animals, both MN cell bodies and axons are visible. In control (Ctrl) and *cekal-1 (RNAi)* animals, commissures appear as single, straight axons directed to the upper side. *cetgs-1* knockdown worms exhibit commissures with extra branching and guidance defects (arrows). (F) Apoptotic autofluorescence signals (arrowheads) in dying MNs of *cetgs-1 (RNAi)* and *cesmn-1 (RNAi Is)* animals. (G) Quantification of dying MNs. Bars represent the average number of dying MNs in transgenic animals from at least two independent lines/clones  $\pm$  SEM. Numbers within and next to bars are the animals tested. \*\*\*\* $P < 0.0001$  (one-way ANOVA). No statistically significant differences were observed by comparing: *cesmn-1 (RNAi)* and *cetgs-1 (RNAi)* ( $P = 0.27$ ) or *cesmn-1 (RNAi)* and *cesmn-1 (RNAi Is)* ( $P = 0.08$ ). (H) RT-qPCR showing the overexpression of *cetgs-1* in *cesmn-1 (RNAi Is); cetgs-1* animals, driven by the pan-neuronal *punc-119* promoter ( $>10$ -fold higher than in the wild type). The reduction in *cetgs-1* expression could not be detected in *cetgs-1 (RNAi)* animals, as silencing occurs in 19 neurons that represent just 0.6% of total cells. Data are from three biological replicates, are normalized to *ceact-1* and are relative to wild-type animals (Ctrl). \*\*\*\* $P < 0.0001$  (one-way ANOVA).

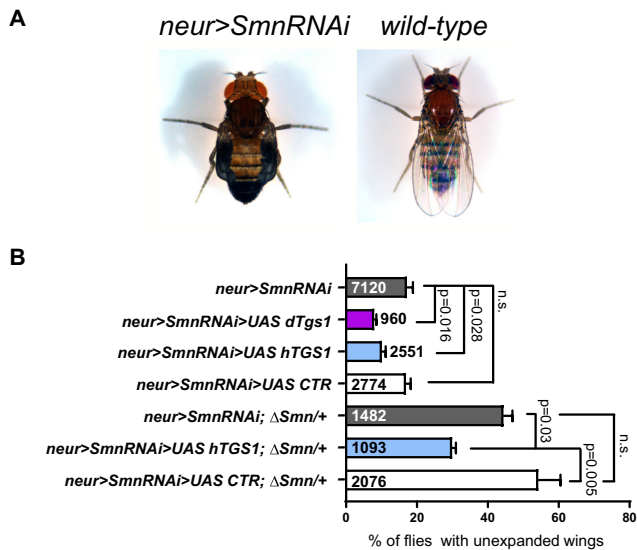


**Figure 2.** *Tgs1* overexpression ameliorates the wing expansion defects caused by neuronal knockdown of *Smn* in *Drosophila*. (A) Examples of flies showing wing expansion failure upon *nsyb-GAL4*-driven (*neur>*) *Smn* RNAi. (B) Frequencies of the defective wing expansion phenotype in flies co-expressing a *UAS-Smn RNAi* (*Smn RNAi*) construct and the indicated *UAS* constructs driven by *nsyb-GAL4* (*neur>*). *UAS dTgs1* encodes GFP-tagged dTgs1; *UAS hTGS1* encodes GFP-tagged human TGS1; *UAS CTR* is a control construct expressing the unrelated Mst protein.  $\Delta Smn/+$  flies are heterozygous for a deficiency of the *Smn* locus. Error bars:  $\pm$  SEM. Numbers within and next to bars are the animals tested. *P*-values: one-way ANOVA with Tukey's multiple comparisons test.

by *nsyb-GAL4*. As control, we used flies carrying a *UAS-CTRL* construct encoding the unrelated Mst protein (38). An increase in the dosage of dTgs1, but not of Mst, significantly lowered the frequency of flies with unexpanded wings (from 16% to 9%) (Figure 2B). A human *TGS1* transgene (*UAS-hTGS1*), which fully rescues the lethality associated with null *dTgs1* mutations (40), decreased the proportion of flies with unexpanded wings from 16% to 10% in *UAS-Smn-RNAi; Smn<sup>+</sup>/Smn<sup>+</sup>* flies, and from 44% to 30% in *UAS-Smn-RNAi* flies bearing a single copy of *Smn* (Figure 2B). These results indicate that dTgs1 overexpression partially suppresses the defects caused by *Smn* deficiency in at least a subset of fly neurons, and that human TGS1 can substitute for the neuronal function of its fly ortholog.

### TGS1 down-regulation in zebrafish causes motor axon defects

To determine the consequences of TGS1 loss in a vertebrate model, we exploited zebrafish. To down-regulate *tgs1*, we injected larvae with two antisense MOs: a translation-blocking MO (*tgs1* ATG-MO) and a splicing-blocking MO (*tgs1* Sp-MO) (Supplementary Figure S2A, B). Each MO was injected at an optimized dosage and caused little or no effect on the overall larval morphology and development (Supplementary Figure S2C).

Injection of 2 ng of *tgs1* ATG-MO resulted in defects in CaP-MN, including axonal truncations and increased terminal branching. A total of 10% of the CaP-MNs exhibited truncated axonal projections and 25% showed increased terminal branching (Figure 3A, B). Negligible CaP-MN de-

fects were observed in uninjected larvae and in larvae injected with a non-targeting MO (Figure 3A, B). A 1.5 ng aliquot of *tgs1* Sp-MO injection led to 15% of CaP-MNs with axonal truncations and 35% with increased terminal branching (Figure 3B). Notably, these results recapitulate the MN defects observed in *smn* morphants (36,72,73).

We also attempted to perform rescue experiments by co-injecting FLAG-tagged human *TGS1* mRNA and the *tgs1* Sp-MO. Co-injection of *tgs1* Sp-MO and 100 pg of *FLAG-hTGS1* mRNA resulted in a significant rescue of the neurological phenotype (Supplementary Figure S2D). However, injection in embryos of *FLAG-hTGS1* mRNA (100–400 pg) caused developmental defects in larvae (Supplementary Figure S2C), preventing a firm conclusion about the rescue capacity of human *TGS1*. Collectively, these results show that the TGS1 function is required for correct MN development in zebrafish.

### TGS1 deficiency impairs 3' processing of snRNAs in human cells

Given the similarity between the phenotypes elicited by TGS1 and SMN depletion, we asked whether TGS1 loss affects snRNP biogenesis (74). To address this, we used two HeLa clones carrying CRISPR/Cas9-induced mutations in *TGS1* (*TGS1 M1* and *M2*) (45), which decrease TGS1 expression to < 10% of the normal level but do not affect the expression of the SMN protein (Figure 4A; Supplementary Figure S3C, D). We have previously shown that both mutant lines exhibit a rather diffuse distribution of the CB marker Coilin (45) and fail to accumulate SMN in CBs, in agreement with previous studies (75). This defect is rescued by the expression of FLAG-TGS1 (*TGS1 M1R* cells, Figure 4A; Supplementary Figure S3A, B). To ascertain whether *TGS1* deficiency affects snRNA expression, we performed RT-qPCR on total RNA from control cells, *TGS1* mutant cells and *TGS1* mutant cells bearing a FLAG-*TGS1* rescue construct. There were no significant differences in the abundance of different snRNAs, with minor changes probably reflecting clonal variability (Figure 4B).

Next, to determine the effects of *TGS1* deficiency on cap hypermethylation of different snRNAs, we performed RIP on total RNA, with the anti-TMG antibody R1131 that specifically recognizes the TMG cap (50,76,77). RT-qPCR on RNA precipitated with the TMG antibody showed that the proportion of TMG-capped U2, U12 and U4atac snRNAs, but not U1 snRNA, was more abundant in control cells than in *TGS1* mutant cells (Figure 4C). The U2 snRNA was the most affected by *TGS1* deficiency, as TMG-capped U2 snRNA molecules in *TGS1 M1* cells were reduced 4-fold compared with the control. TMG-capped U4atac and U12 snRNA molecules were reduced by 50% in *TGS1 M1* cells. In contrast, the abundance of TMG-capped U1 snRNA was not reduced in *TGS1 M1* cells. This observation was confirmed by an independent set of RIP experiments, performed with the anti-TMG antibody K121 (77) and in which gel-purified yeast U1 or U2 snRNAs were added as spike-in TMG-capped RNAs to control for immunoprecipitation efficiency (Supplementary Figure S4A, B). As a positive control for these experiments, we used telomerase RNA (hTR). The abundance of TMG-capped



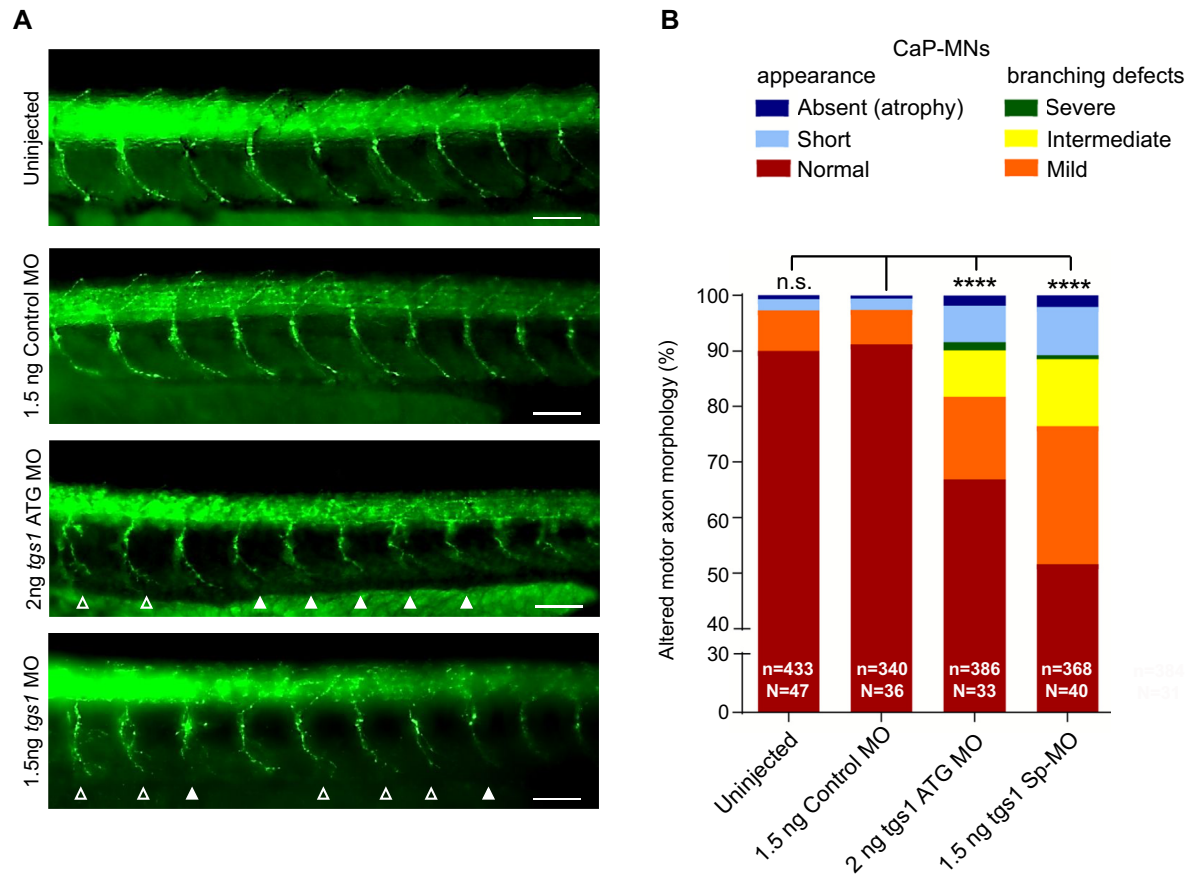


**Figure 3.** *Tgs1* down-regulation in zebrafish leads to defects in CaP-MNs. (A) Lateral views of whole-mount embryos immunostained with a synaptotagmin antibody (Znp1) that labels the CaP-MNs. Embryos were untreated or injected with the indicated MOs. Injection of either *tgs1* ATG-MO or *tgs1* Sp-MO results in truncated or absent motor axons (solid arrowheads) and terminally branched axons (open arrowheads). Scale bar, 25  $\mu$ m. See also Supplementary Figure S2. (B) Based on overall appearance, CaP-MNs were classified as: normal, short (truncated axonal projection) or absent (axonal atrophy). Based on terminal branching, axons were classified as normal, mild (branching ventral from midline), intermediate (2–3 or more branches at ventral or midline) or severe (>3 branches ventral or dorsal from the midline). Zebrafish larvae injected with 1.5 ng of *tgs1* Sp-MO or 2 ng *tgs1* ATG-MO displayed CaP-MN defects compared with control (non-targeting) MOs and uninjected fish. Results are percentages from three independent experiments ( $n$  = axons analysed;  $N$  = animals tested). \*\*\*\* $P$  < 0.0001  $\chi^2$  test; n.s. not significant. See also Supplementary Figure S2D.

hTR was reduced by 50% in *TGS1 MI* cells (Figure 4C), consistent with our previous work showing that *TGS1* hypermethylates hTR and down-regulates its abundance (45). The *GAPDH* and 5.8S RNAs were used as negative controls as *GAPDH* mRNA has an MMG cap that is not recognized by the anti-TMG antibody, and the 5.8S rRNA is normally uncapped. As expected, these RNAs bound very poorly to the anti-TMG antibody and were precipitated in similarly low proportions from both *TGS1 MI* and control cells (Figure 4C). RIP with the anti-TMG antibody, performed on nuclear RNA fractions and followed by northern blotting, confirmed that, compared with control and *TGS1 MIR* cells, *TGS1 MI* cells exhibit a reduction in the TMG-capped U2 snRNA and U3 snoRNA, but not in the U1 snRNA (Figure 4D). This experiment also showed that nuclear extracts of *TGS1 MI* cells are enriched in slower migrating U2 species (Figure 4D), which are likely to correspond to U2 precursors carrying genome-encoded extensions at their 3' ends (11,21).

Next, we analyzed by NB the distribution of the extended snRNA species in nuclear and cytoplasmic fractions of both

control and *TGS1* mutant cells. Extended RNA precursors were detected for U2 snRNAs but not for U1, U3, U4atac and U5 snRNAs. U2 snRNA precursors were clearly enriched in both nuclear and cytoplasmic RNA of *TGS1 MI* and M2 cells, compared with *TGS1*-proficient cells (Figure 4E; Supplementary Figure S5A, B). Nuclear or cytoplasmic accumulations of extended U2 precursors were not enriched in cells carrying mutations in *TCABI* (48) that disrupt CB stability (Figure 4E). Immunostaining of *TGS1 MI* cells with antibodies against the TMG cap and the SmB protein showed a strong reduction in the speckled nuclear distribution of snRNPs compared with control or *TGS1 MIR* cells (Supplementary Figure S5C). In addition, after immunostaining with these antibodies, *TGS1 MI* nuclei showed a diffuse cytoplasmic halo that was not observed in control or *TGS1 MIR* cells, suggesting that *TGS1* deficiency leads to retention of some snRNPs in the cytoplasm (Supplementary Figure S5C). Consistent with this finding, single-molecule FISH detected cytoplasmic retention of U2 species in *TGS1 MI* cells but not in *TGS1*-proficient cells (Supplementary Figure S5D). In contrast, FISH anal-

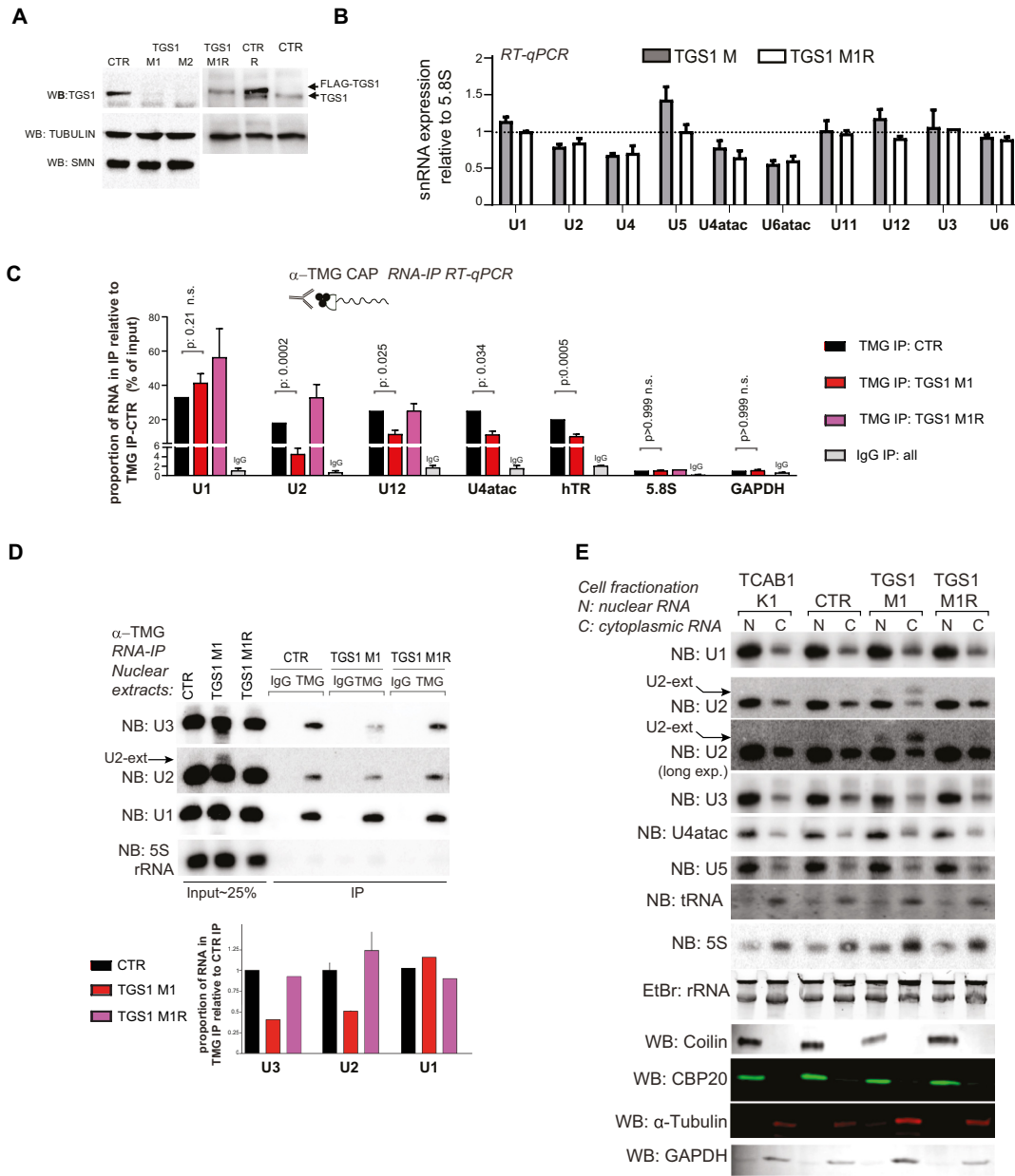


**Figure 4.** TGS1 deficiency affects maturation of U2 snRNAs in human cells. **(A)** Western blotting (WB) showing TGS1 expression in two independent CRISPR clones of HeLa cells (M1, M2). CTR is the parental cell line; *TGS1 M1R* and *CTR R* are a *TGS1 M1* and a parental line stably expressing FLAG-TGS1. Tubulin is a loading control. The abundance of the SMN protein is not affected by mutations in *TGS1* (see also Supplementary Figures S3C, D and S6B). **(B)** RT-qPCR showing the abundances of the indicated snRNAs in *TGS1 M1*, *TGS1 M2* (collectively indicated as *TGS1 M*) and *TGS1 M1R* cells. Data from three independent experiments are relative to parental HeLa cells (set to 1) and normalized to 5.8S rRNA. The U3 snoRNA (U3) and the uncapped U6 and U6atac snRNAs are controls. No statistically significant differences were observed between *TGS1 M* and *TGS1 M1R* cells (error bars:  $\pm$  SEM; *P*-values: all  $> 0.05$ ; two-way ANOVA with Sidak's multiple comparisons test). **(C)** Total RNA from control (CTR), *TGS1 M1* and *TGS1 M1R* cells was precipitated with the R1131 anti-TMG CAP antibody (50,76,77) (TMG IP) or control IgGs (IgG IP). Histogram bars represent the fold enrichment of the indicated transcripts in RIP eluates (relative to input), determined by RT-qPCR and normalized to TMG IP from control cells (expressed as the percentage of input). IgG IP bar: values of IgG IPs for the three cell types were pooled into a single bar. MMG-capped GAPDH mRNA and the uncapped 5.8S rRNA are negative controls. Data are from 3–5 independent experiments. *P*-value: two-way ANOVA with Sidak's multiple comparisons test. See also Supplementary Figure S4A and B. **(D)** RIP was performed with the R1131 anti-TMG antibody (TMG) or control IgG on nuclear extracts from control (CTR), *TGS1 M1* and *TGS1 M1R* cells. Membranes were probed for U3 snoRNA, U2 and U1 snRNAs; the 5S rRNA, which lacks a TMG cap, is a negative control. Histogram bars represent the quantification of the U2, U1 and U3 RNAs, by densitometric analysis. Data are from three biological replicates. Note the presence of U2 snRNA precursors (arrow) in nuclear extracts from *TGS1 M1* cells, which display reduced hypermethylation of U2 snRNA and U3 snoRNA, but not of U1 snRNA. **(E)** Representative northern blots showing U2 snRNA precursors (arrow) in nuclear and cytoplasmic fractions. RNA was purified from nuclear and cytoplasmic fractions from: *TCAB1 K1* HeLa mutant cells [this cell line, described in (48) has reduced CBs and was used as a control]; CTR, parental HeLa cells; *TGS1 M1* and *TGS1 M1R* cells. Membranes were probed for the U1, U2, U4atac, U5 snRNA and the U3 snoRNA. 5S rRNA and tRNA-Arg were used as loading controls. EtBr rRNA staining is a loading control. Western blots with Coilin, CBP20, alpha-tubulin and GAPDH were used as loading controls.

ysis showed that the nuclear localization of U1 snRNA is unaffected by TGS1 deficiency (Supplementary Figure S5D). These results indicate that TGS1 deficiency causes aberrant accumulation of unprocessed U2 precursors that might interfere with spliceosome activity, as occurs in yeast (78).

We characterized the 3' ends of the pre-U2 molecules in total RNA by 3' rapid amplification of cDNA ends (RACE) and next-generation sequencing as previously described (47,79). In control cells, 90% of the reads mapped to the mature forms of U2, most of which contained 188 nt plus a 3' adenosine added post-transcriptionally ( $\leq 189$  nt), in agreement with previous results (3,80). The remaining 10% of the U2 molecules had extended tails including genome-encoded nucleotides at their 3' ends (Figure 5A, B). *TGS1* mutants displayed a 4-fold higher proportion of 3'-extended U2 molecules (41%) compared with control (10%), with an average tail length of 12 nt (Figure 5A, B). In *TGS1* *MIR* cells, the abundance of the extended U2 molecules was reduced from 41% to 20%, showing rescue of the mutant phenotype (Figure 5A). 3' RACE and sequencing performed on nuclear and cytoplasmic RNA confirmed the data obtained by northern blotting (Figures 4D, E and 5C, D). In the nuclear RNA fractions, the abundance of the U2 extended species was 18% in *TGS1* mutant cells, 7% in control cells and 8% in *TGS1* *MIR* cells (Figure 5C). In the cytoplasmic fractions, the extended U2 molecules were 52% in *TGS1* mutant cells, 13% in control cells and 20% in *TGS1* *MIR* cells (Figure 5C). *TGS1* mutant cells showed no variations in the proportion of mature U2 molecules carrying a 3'-untemplated adenosine compared with controls; in both cases, the 189/188 ratio was  $\sim 80\%$ . Importantly, the finding that the nuclei of *TGS1* mutant cells contain more extended U2 molecules than control nuclei (Figures 4D, E and 5C) suggests that a fraction of these unprocessed species completes the cytoplasmic assembly pathway and is imported in the nucleus.

To assess whether TGS1 deficiency affects processing of the U2 precursors in a different cell type, we knocked down *TGS1* by RNAi in UMUC3 cells, which showed a strong reduction in the TGS1 protein and defective CBs (Supplementary Figure S3E, F). 3' RACE and sequencing on total RNA revealed that in *TGS1*-RNAi cells the proportion of extended molecules is 3-fold higher than in cells treated with control siRNA (Figure 5A).

To confirm that the extended species are precursors of U2 molecules, we performed metabolic labeling of newly transcribed RNA with 4-thiouridine for 4 h in control HeLa cells, and affinity-purified this nascent RNA population with thiol-specific biotinylation and streptavidin-coated magnetic beads (47). Unlabeled RNAs (steady-state RNA) recovered after this treatment are enriched in mature RNA species, while labeled RNAs are enriched in short-lived RNA precursors. A comparison of the sequence profiles showed that extended U2 molecules are 5-fold more abundant in nascent RNA samples (59% of total U2 reads) than in steady-state RNA (12%; Figure 5A, B), indicating that the extended U2 species are immature U2 precursors, not yet processed at their 3' ends.

In total RNA from control cells, a small fraction of the U2 reads are extended molecules carrying non-

templated adenosines (0.2%) or uridines (0.6%) added post-transcriptionally at their 3' ends. The acquisition of an extra A or U is specific for the extended molecules with a mean tail length of 12 nucleotides. In *TGS1* mutant cells, the fraction of extended U2 molecules incorporating extra uridines is six times and twice higher than in control and *TGS1* *MIR*-rescued cells, respectively (Figure 5B, E). A 5-fold increase in uridylated molecules is also observed in *TGS1* RNAi UMUC3 cells compared with cells treated with non-targeting double-stranded RNA (dsRNA) (Figure 5E). These data suggest that TGS1 affects not only 3' trimming but also the profile of post-transcriptional modifications on the U2 precursors. Interestingly, oligo(U)-extended molecules are 5-fold more abundant in nascent RNA than in mature RNA, indicating that these modifications represent an intermediate step in the 3' processing of U2 precursors (Figure 5E).

We also analyzed the 3' sequences of the U1 and U4atac snRNAs. In both control and *TGS1* mutant cells, 98% of U1 snRNA molecules were 164 nt long and  $< 1\%$  of these molecules carried untemplated adenosine or uridine residues at their ends, indicating that in the *TGS1* mutant clones, neither cap hypermethylation of U1 snRNAs nor their biogenesis is affected (Supplementary Figure S4C). In contrast, *TGS1* mutant cells were enriched in U4atac-extended forms, showing a mean tail length of 10 nt; these forms were 19% of total reads in *TGS1* mutants, 6% in control cells and 9% in rescued cells (Figure 5F, G). Moreover, in *TGS1* mutant cells, 3% of U4atac molecules incorporated additional uridines, compared with 0.25% in control cells and 0.7% in rescued cells (Figure 5H).

Collectively, these results indicate that TGS1 depletion results in defective hypermethylation of some snRNA species, which largely correlates with the accumulation of extended U2 and U4atac snRNA molecules. These snRNAs differ in the type and proportion of 3' end extensions, most probably reflecting diverse dynamics in their 3' end processing.

### Tgs1 controls 3' processing of snRNAs in *Drosophila*

To ask whether the role of TGS1 in snRNA 3' processing is conserved in flies, we exploited *dTgs1<sup>RI</sup>*, a null CRISPR/Cas9-induced allele, which in homozygosity causes death in late second instar larvae (40). We also used *dTgs1<sup>RI</sup>/dTgs1<sup>CB0</sup>* heterozygous flies that die as third instar larvae. The lethality of both mutants is rescued by ubiquitous expression of either a *dTgs1* or a human *TGS1* transgene (40,42).

We characterized the 3' ends of U2 snRNAs by 3' RACE and RNA sequencing on total RNA from wild-type larvae (*CTR*), *dTgs1<sup>RI</sup>* homozygous larvae and *dTgs1<sup>RI</sup>/dTgs1<sup>CB0</sup>* larvae; as control, we also examined mutant larvae constitutively expressing *dTgs1*. *dTgs1* mutant larvae showed an increase in 3'-extended U2 species compared with either wild-type larvae or larvae bearing the rescue construct (Figure 6A). A total of 95% of these extended U2 species displayed one additional uridine at the 3' end (Figure 6B). The remaining 5% of the extended molecules included species containing longer tails incorporating both genome-templated



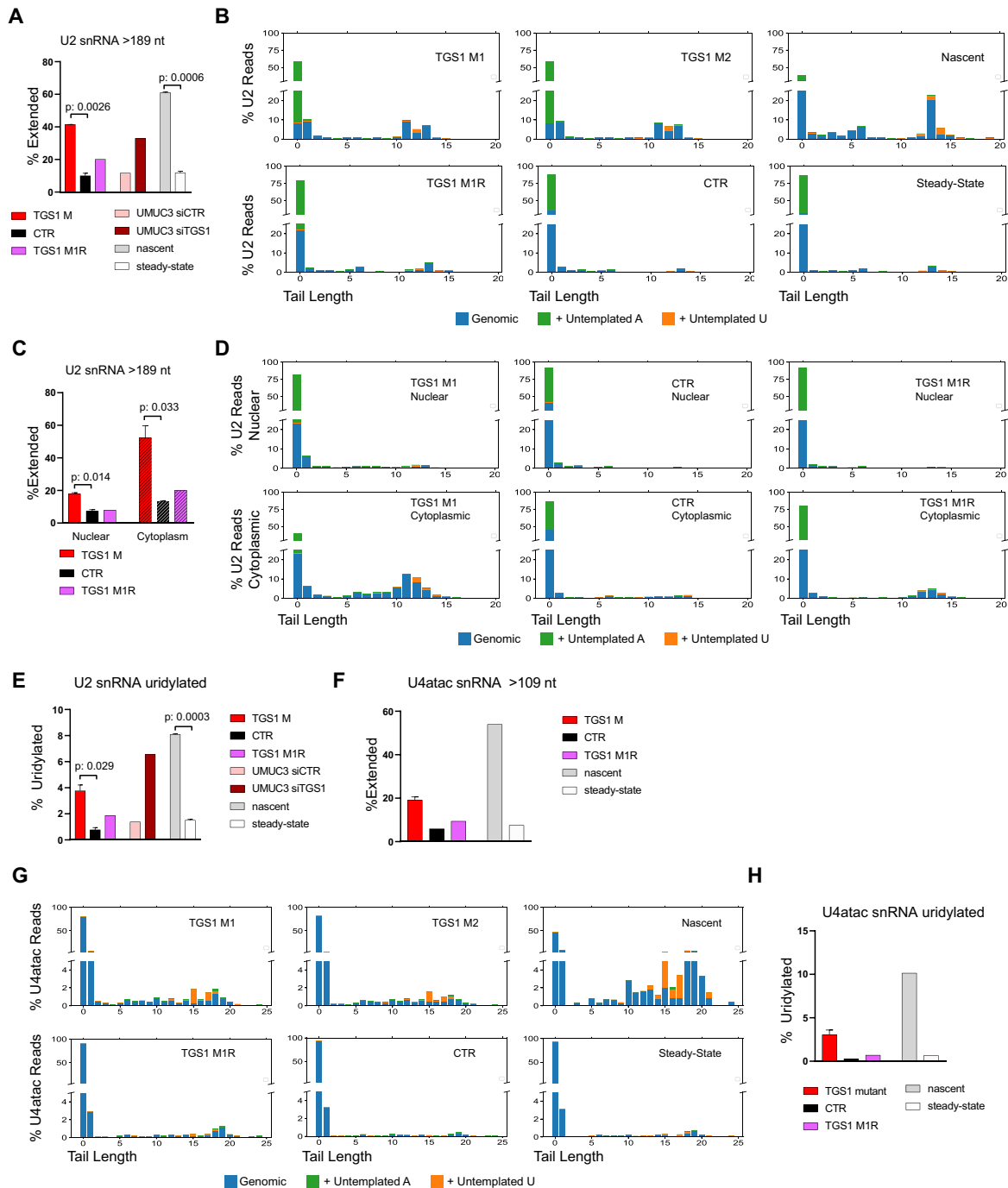


**Figure 5.** TGS1 loss leads to an accumulation of 3'-extended U2 and U4atac snRNAs in human cells. (A) 3' RACE and sequencing on total RNA showing that *TGS1* mutant HeLa cells accumulate more U2-extended snRNA molecules than either parental (CTR) or *TGS1 M1R* cells. UMUC3 cells treated with TGS1 siRNAs (siTGS1) also accumulate more U2-extended snRNAs than cells exposed to non-targeting siRNAs (siCTR). Nascent and steady-state RNA fractions were purified from control HeLa cells (see the Materials and Methods). Extended U2 molecules carry extra 3' sequences of templated and/or untemplated nucleotides. Average reads per sample  $> 78\,000 \pm 41\,000$ . Data are mean values of two independent clones + SEM. *P*-values: two-sided Student's *t*-test. (B) Plots showing the percentage of the different sequence reads of U2 snRNAs in the same HeLa cell samples as in (A). Numbers on the *x*-axis: additional nucleotides beyond the 189 nt of the mature form. Position 0 includes mature U2 snRNA species of 188 nt or 188 nt plus a post-transcriptionally added A. *y*-axis: percentage of total reads. Blue, genomic-templated nucleotides; green, untemplated adenosine; orange, untemplated uridine. (C) Characterization of U2 snRNA molecules from nuclear and cytoplasmic fractions from *TGS1 M1*, *TGS1 M2*, *TGS1 M1R* and control (CTR) cells. (D) Tail length and composition of U2 snRNAs in the samples shown in (C). *y*-axis: percentage of total reads. (E) Percentages of U2 molecules with tails ending with post-transcriptionally added uridines in the HeLa cell RNA samples described in (A). Total reads per sample  $> 75\,000$ . (F) Percentages of 3'-extended U4atac snRNAs in the RNA samples described in (A). Average reads per sample  $> 106\,000 \pm 21\,000$  (Nascent:  $> 11\,000$ ). (G) Tail lengths and composition of the 3' ends of U4atac snRNAs in *TGS1 M1*, *TGS1 M2*, *TGS1 M1R* and control (CTR) cells. Numbers on the *x*-axis: additional nucleotides beyond the 130 nt of mature U4atac (position 0). *y*-axis: percentage of total reads. (H) Percentages of U4atac snRNA molecules with extended tails ending with untemplated uridines. Total reads per sample  $> 75\,000$ .

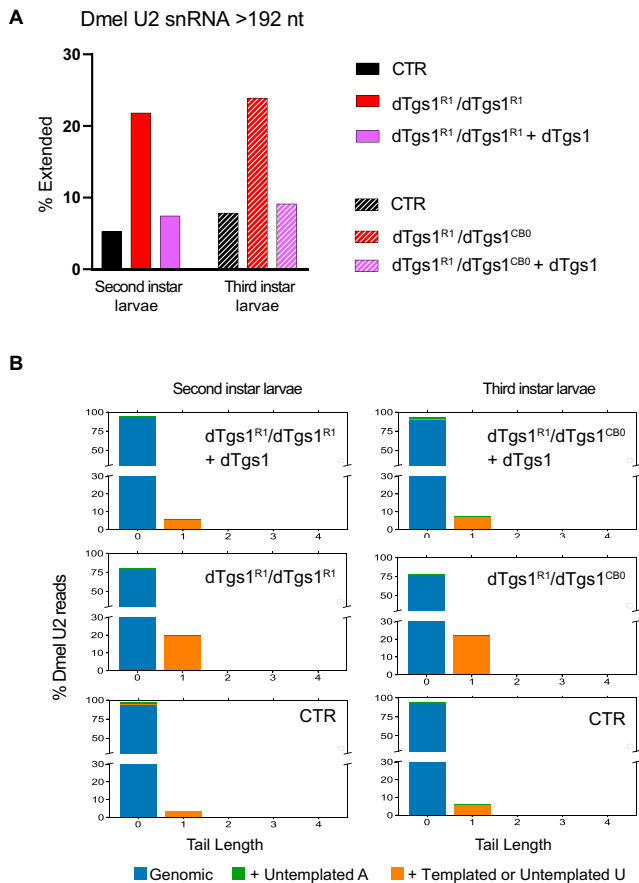


**Figure 6.** 3'-Extended U2 snRNA molecules accumulate in *Drosophila dTgs1* mutants. **(A)** Percentage of extended U2 snRNA molecules determined by 3' RACE and sequencing on RNA from equally aged second or third instar mutant larvae, rescued mutant larvae (bearing a *dTgs1* construct) and wild-type larvae (CTR). The most abundant population of U2 snRNAs is 192 nt long. Extended U2 snRNAs are longer than 192 nt and incorporate templated or untemplated nucleotides at their 3' ends. Total reads > 2900. **(B)** Tail length and composition of the 3' ends of U2 snRNAs for the second and third instar larvae described in (A). Numbers on the x-axis: additional nucleotides beyond the mature form of 192 nt (position 0). y-axis: percentage of total reads.

and untemplated A or U nucleotides. Thus, TGS1 is required for proper 3' processing of U2 snRNAs also in flies.

In contrast, an analysis of the U1 snRNAs showed that they are substantially unaffected by *dTgs1* mutations, consistent with the results obtained with human cells. In mutant and wild-type larvae, extended species represented ~1.5% and 0.5% of total U1 RNAs, respectively.

#### Aberrant transcripts accumulate in both *TGS1* and *SMN* mutant cells

Studies conducted in different systems demonstrated that SMN deficiency causes profound perturbations in the transcriptome (81–86). To explore the consequences of TGS1 loss on mRNA splicing and gene expression, we performed deep sequencing on total RNA extracted from *TGS1* mutant HeLa cells, and from two independent *SMN* mutant clones derived from the same HeLa cell line used to generate *TGS1* mutant cells. These lines, designated as *SMN*

*C1* and *SMN C2*, carry CRISPR-induced mutations in the sixth exon of the gene and produce mutated versions of the SMN protein, which are expressed at reduced levels, compared with full-length SMN (Supplementary Figure S6A, B). These lines have normal amounts of the TGS1 protein (Supplementary Figure S6B) and do not exhibit significant changes in viability, compared with the HeLa parental cell line (CTR) and *TGS1 M1* mutant cells (Supplementary Figure S6C). *SMN C1* has a small deletion in the SMN proline-rich domain and *SMN C2* carries frameshift mutations (see Supplementary Figure S6A). The SMN proteins encoded by the *SMN C2* cells have a lower molecular weight compared with the wild-type protein. The *SMN C1* and *SMN C2* mutant cells are defective in CB formation and exhibit fewer SMN-enriched CBs compared with control cells (Supplementary Figure S6D, E).

Paired-ended Illumina sequencing (160 million reads/sample) was performed on RNA isolated from *TGS1* mutant clones (*M1* and *M2*), *SMN* mutant clones (*C1* and *C2*) and parental HeLa cells (CTR). Independent mutant clones and controls were clustered based on both transcript and gene expression profiles (Supplementary Figure S7A–C). We used Kallisto (87) and Sleuth (57) for transcript quantification and differential analysis, respectively (see the Materials and Methods). *TGS1* and *SMN* mutant cells showed a differential expression of both annotated and unannotated transcripts compared with controls [reconstructed by Scallop (56); Figure 7A, B; Supplementary Table S1]. Our analysis revealed significant changes in the expression levels of 3084 and 351 transcript isoforms in *TGS1* and *SMN* mutant cells, respectively (Figure 7A, B; Supplementary Table S1). We found changes in the expression levels of many unannotated transcripts (1080/3084 for *TGS1* and 158/351 for *SMN* mutants); 48 of these novel isoforms were found to be affected in both mutant cell types (Figure 7C; Supplementary Table S1). The number of differentially expressed transcripts was higher in *TGS1* mutant cells than in *SMN* mutant cells (Figure 7A–C), probably reflecting the higher degree of functional inactivation of *TGS1* compared with *SMN* (Figure 4A; Supplementary Figure S6A, B).

The numbers of annotated and unannotated transcripts that were found to be differentially expressed in both *SMN* and *TGS1* mutant cells were significantly greater than would be expected by chance ( $P$ -value <  $10e^{-22}$ , hypergeometric test, 110 400 total annotated transcripts, 28 100 total unannotated transcripts with computed  $P$ -value by Sleuth) (Figure 7C; Supplementary Table S1; see the Materials and Methods). Notably, 71% and 76% of the differentially expressed unannotated transcripts found in *TGS1* and *SMN* mutant cells, respectively, showed an increased number of reads for intergenic regions compared with controls (Figure 7A, B; Supplementary Table S1). These 3'-elongated transcripts extended beyond the 3' end of the gene and sometimes included the coding region of the next gene, probably reflecting an altered transcription termination. Most of the differentially expressed transcripts were also identified using an independent analysis workflow (56,59) (Supplementary Tables S3–S5). The mutant cells also exhibited changes in splicing behavior (Supplementary Figure S8A), with intron retention (IR) being the most frequent defect in both

*TGS1* (3.5% and 4.5% of annotated and unannotated IR events, respectively) and *SMN* mutants (1.2% and 2.1% of annotated and unannotated IR events, respectively); Figure 7D–F; Supplementary Figure S8A, B and Supplementary Table S2.

Long-read Oxford Nanopore sequencing was performed on the six RNA samples, described above, to gain additional information on the transcripts that accumulate in *TGS1* and *SMN* mutant cells, and to assess the association of splicing defects and 3' extensions on the same transcript isoform. In total, 72 million reads were generated, pre-processed and mapped to the human genome. The FLAIR pipeline (61) was employed for splicing junction correction, yielding 24.7 million corrected multi-exonic reads that were used for transcriptome reconstruction (see the Materials and Methods and Supplementary Figure S9). A total of 55 815 transcripts, 41 565 of which were not present in the reference annotation, were identified and quantified using FLAIR; differential splicing between mutant and control samples was assessed using SUPPA2 (Figure 8A–C; Supplementary Figure S10A). The number of shared annotated and unannotated differential splicing events between *SMN* and *TGS1* mutant cells is greater than expected by chance (Figure 8D). Furthermore, there is a significant overlap between the differential splicing events identified by Illumina and Nanopore sequencing (Figure 8E; Supplementary Table S8), providing further support for the reproducibility of our findings on the global splicing defects caused by *TGS1* and *SMN* depletion. Multi-exonic reads intersecting the last exon of each gene were used to identify loci in which the proportion of readthrough transcripts was significantly different in *TGS1* and *SMN* mutant samples compared with control (Figure 8F; Supplementary Table S9). Interestingly, in both comparisons, most of the differential readthrough events consist of a higher proportion of readthrough reads in the mutant, indicating a defective termination leading to the production of longer transcripts. Many of these longer transcripts extended into the downstream gene. For the genes showing such preferential readthrough in mutant samples, SUPPA-2 was used to determine the number of readthrough and non-readthrough reads harboring an alternative splicing event in the mutant samples. These analyses (Figure 8G; Supplementary Figure S10B; Supplementary Table S10) indicate that in both *TGS1* and *SMN* mutant cells, readthrough reads have a higher probability of also containing an alternative splicing event compared with non-readthrough reads.

To confirm the results obtained using high-throughput data analysis, we performed targeted validation for four transcripts by RT-PCR or RT-qPCR on RNA samples from CTR, *TGS1M* and *TGS1MIR* cells. Amplification products consistent with the predicted novel transcript isoforms were enriched in the two *TGS1* mutant clones compared with both the parental cell line and *TGS1 MIR* cells (Supplementary Figures S11 and S12). Two of these validated novel transcripts were found to be enriched in *TGS1* mutant clones also by Nanopore analysis and are representative examples of readthrough transcripts that extend into the downstream gene (Supplementary Figure S11B, E).

## DISCUSSION

We have shown that the highly conserved *TGS1* hypermethylase localizes to MNs in *C. elegans*, and that its deficiency results in morphological and functional abnormalities in neurons from both *C. elegans* and *D. rerio*. Consistent with these defects, *TGS1* deficiency impairs locomotion in worms and wing expansion in flies, which is governed by bursicon-expressing neurons (88). Previous work has also shown that mutations in *Drosophila Tgs1* cause abnormal larval locomotion (40,69,70). The phenotypes elicited by *TGS1* inhibition in flies, worm and zebrafish are highly reminiscent of those caused by loss of function of the *SMN* gene. Importantly, we showed that *TGS1* overexpression ameliorates the neurological phenotypes elicited by the impairment of the *SMN* function in both fly and worm model systems. These findings suggest commonalities in the molecular and cellular effects induced by either *TGS1* or *SMN* loss of function.

Our investigation on the consequences of *TGS1* loss in snRNA biogenesis uncovers the involvement of this hypermethylase in 3'-end processing. The HeLa cell model was instrumental to compare the molecular consequences of *SMN* and *TGS1* loss in the same isogenic background. Additionally, we demonstrate that 3'-extended mRNA transcripts accumulate in both *TGS1* and *SMN* mutant cells. Lastly, our analyses of different animal models provide robust evidence that *TGS1* together with *SMN* plays a conserved, important role in neuronal function.

Several studies have linked neurodegeneration to defective snRNA processing, snRNP biogenesis and/or pre-mRNA splicing (3,74,85,89,90). It has been reported that *SMN*-depleted cells exhibit an enrichment of 3'-unprocessed snRNA precursors resulting from their impaired assembly into snRNPs (11). In a mouse model of SMA, MNs display a much greater reduction in the snRNPs levels relative to unaffected spinal cells (91), and their selective death is the result of converging mechanisms of p53 activation driven by dysregulation of distinct mRNA splicing pathways (92–94). It has been also reported that mutations in a single gene of the U2 multicopy cluster (*Rnu2-8*) result in defective splicing and cause ataxia and neurodegeneration in mice (89). Unprocessed snRNAs accumulate in cells from patients affected by PCH7, which is also characterized by MN loss (3). Interestingly, we show that *TGS1* mutant cells accumulate extended snRNA species with post-transcriptionally added adenosines or uridines similar to cells from PCH7 patients (3,95,96).

Our 3' RACE and sequencing experiments show that *TGS1* loss results in the accumulation of untrimmed 3'-extended U2 snRNA molecules, but has no effect on U1 snRNA in both human cells and *Drosophila* lethal mutants. *TGS1*-deficient human cells also accumulate untrimmed U4atac snRNAs. Interestingly, viable hypomorphic *Drosophila Tgs1* mutants that cause male sterility exhibit a reduction in TMG-capped U1 and U2 snRNAs in testes and a concomitant accumulation of long precursors for most snRNAs (97). Collectively, these results indicate that *TGS1*-mediated cap hypermethylation affects 3'-end processing of snRNAs.



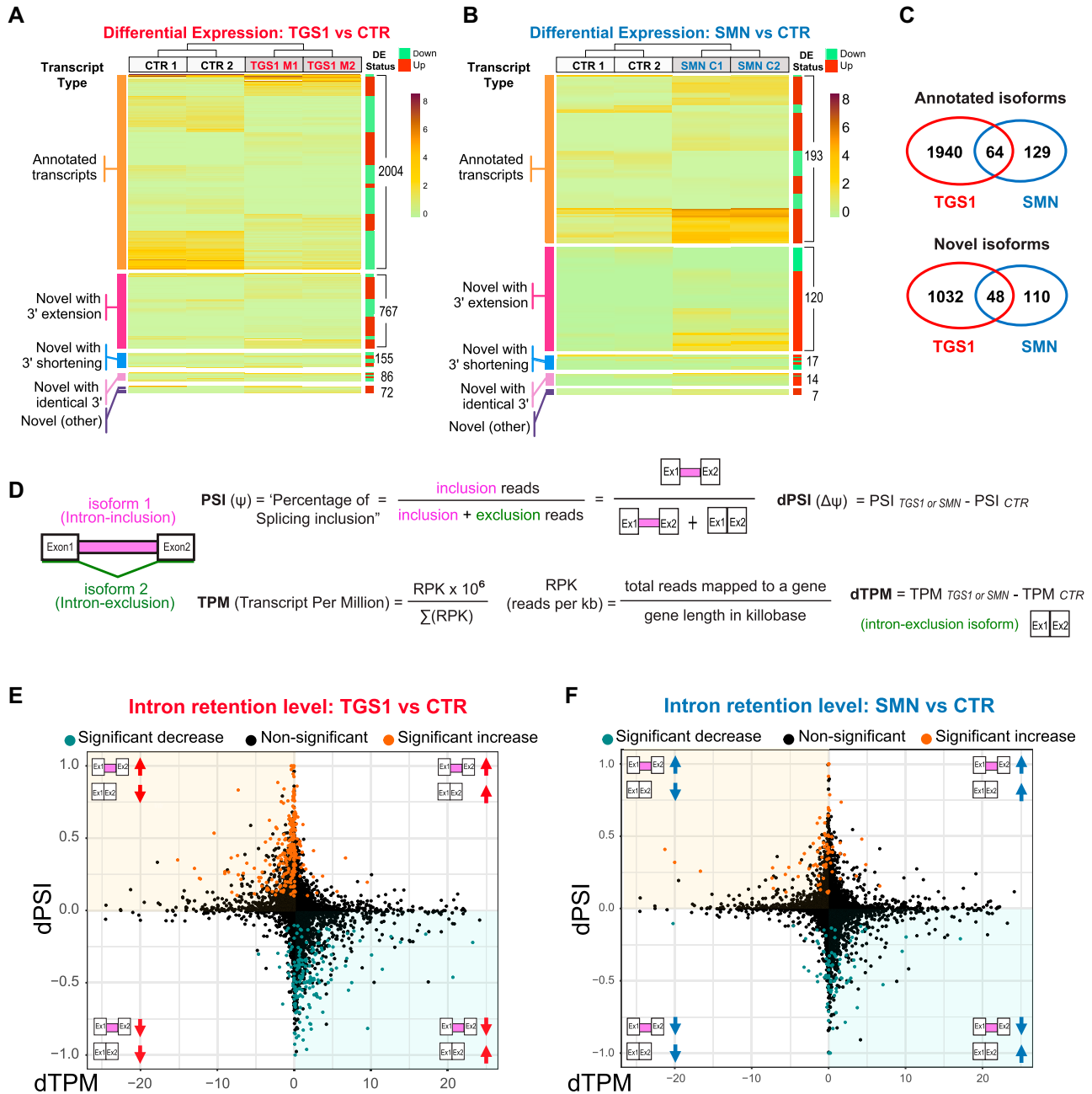


**Figure 7.** Mutations in *TGS1* and *SMN* cause global changes in RNA expression and splicing. (A, B) Heatmaps depicting the expression levels (TPM values estimated by Kallisto) for differentially expressed (DE) transcripts in *TGS1 M1* and *TGS1 M2* (A), or *SMN C1* and *SMN C2* (B) mutant cells, compared with parental HeLa cells (CTR). Transcripts are classified into five types: annotated transcripts per GENCODE (orange); novel transcripts with extended 3' (magenta) or shortened 3' (blue); novel transcripts with annotated identical 3' (pink); and other (intergenic and opposite-strand) novel transcripts (purple). Transcripts within each group are ranked by unsupervised clustering. Total transcript number for each group and the DE status for each transcript (either up- or down-regulated in mutant cells) are annotated by the green/red sidebar to the right (see also Supplementary Table S1). (C) Venn diagram from data in (A) and (B), showing the significant number of shared DE transcript isoforms (both annotated and unannotated) between *TGS1* and *SMN* mutant cells. See also Supplementary Table S1. (D) Methodological approach used for quantification of intron retention (IR) levels (see also the Materials and Methods). (E, F) Scatter plots showing for each IR event between mutant (*TGS1 M1* and *M2* or *SMN C1* and *C2*) and CTR cells the differential PSI (dPSI) against the differential expression level (dTPM) of the major transcript (intron exclusion). The significant IR events are color-coded in the plots, with significantly up-regulated events colored in orange and significantly down-regulated in teal.

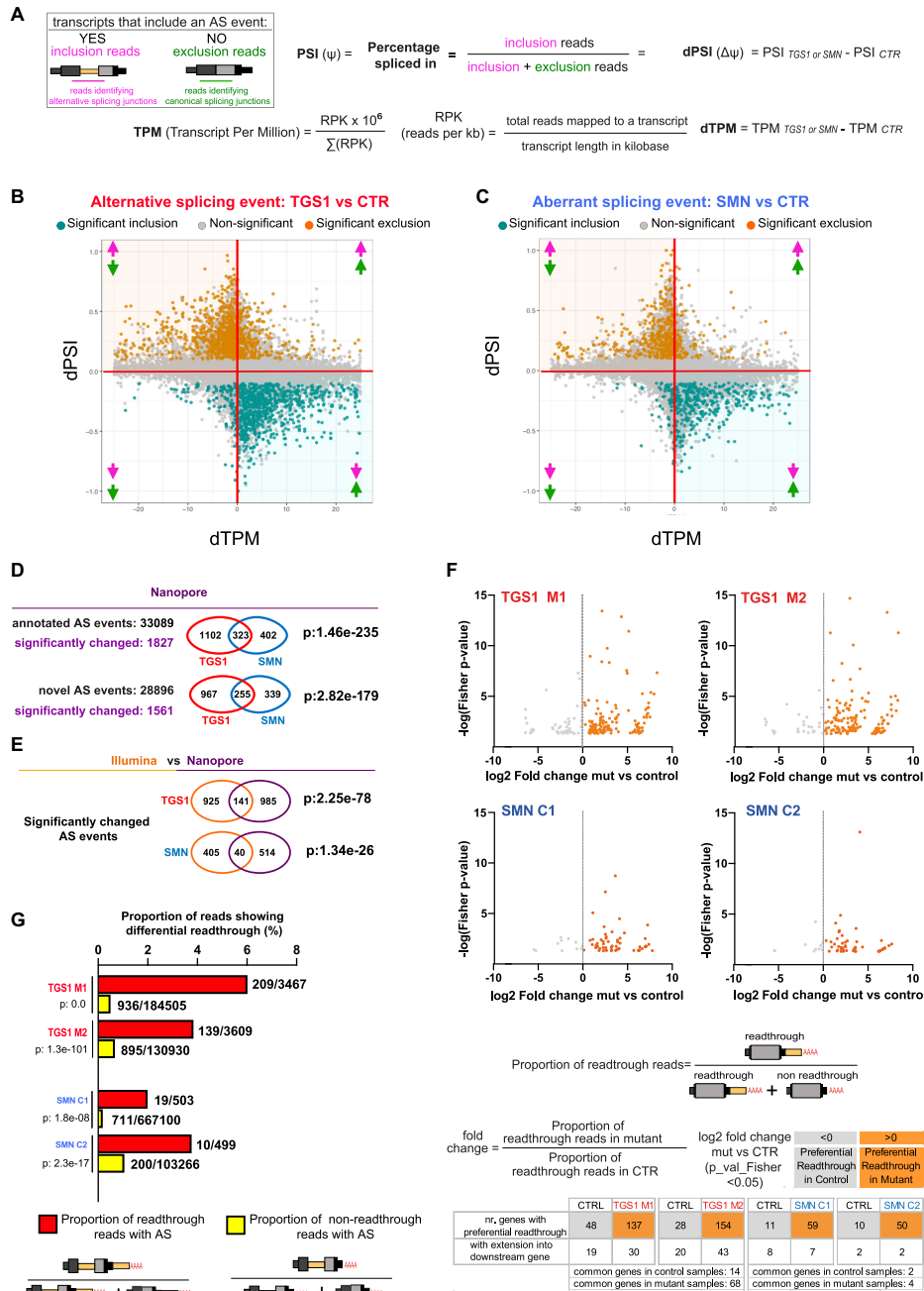


**Figure 8.** Analysis of the aberrant transcripts that accumulate in *TGS1* and *SMN* mutant cells by Oxford Nanopore sequencing. **(A)** Methodological approach used for transcript quantification and evaluation of transcript differential splicing. **(B,C)** Scatter plots showing, for each AS event between mutant (*TGS1 M1, M2* and *SMN C1, C2*) and parental HeLa cells (CTR), the differential PSI (dPSI) against the differential expression level (dTPM) of the major transcript (that does not contain the AS event). The significant differential splicing events are color-coded in the plots, with significantly included events colored in orange and significantly excluded events in teal. Non-significant events are in gray (see also Supplementary Figure S10A for a classification of the AS events and Supplementary Table S6). The arrows indicate up- or down-regulation of AS inclusion transcripts (pink) and AS exclusion transcripts (green), as depicted in (A), respectively. **(D)** Venn diagrams showing the number of annotated and novel differential splicing events found in *TGS1 M1, M2* and *SMN C1, C2* mutant cells by Nanopore sequencing. The statistical significance of the intersection was determined via Fisher's exact test. See also Supplementary Table S7. **(E)** Venn diagram showing the number of the differential splicing events identified by Illumina and Nanopore analysis in *TGS1* and *SMN* mutant cells. The statistical significance of the intersection was determined via Fisher's exact test. See also Supplementary Table S8. **(F)** Dot plots showing differential readthrough events in mutant cells (orange dots) versus control cells (gray dots). For each readthrough event, the value of the log<sub>2</sub>(fold change) (mutant versus control) is reported on the x-axis. Statistical significance of the fold enrichment for each event was determined by Fisher's exact test (*P*-values on the y-axis; *P* < 0.05 was considered significant). The numbers of genes with 'Preferential Readthrough in Mutant' (orange) or 'Preferential Readthrough in CTR' (gray) are reported below the graphs. See also Supplementary Table S9; and the Materials and Methods. **(G)** Bar plot showing that, in mutant samples, the percentage of reads that carry an aberrant splicing event is higher among readthrough reads compared with non-readthrough reads. Only reads mapping to the last exons undergoing 'Preferential Readthrough in Mutant' events were used for this analysis. Aberrant splicing was assessed by comparing reads from mutant samples against non-readthrough reads from control samples. The significance of the difference in the proportions of aberrant splicing reads between readthrough and non-readthrough reads was assessed using the  $\chi^2$  test. See also Supplementary Table S10.

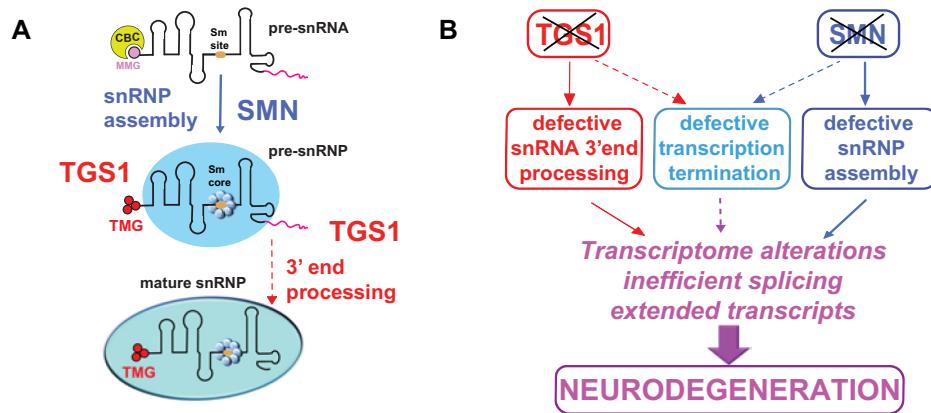


**Figure 9.** SMN and TGS1 protect against neurodegeneration through both common and specific routes. (A) Roles of SMN and TGS1 in snRNA biogenesis. The dashed arrow line indicates that the role of TGS1 in 3'-end processing could be indirect. (B) A model for the roles of TGS1 and SMN in prevention of neurodegeneration. The effects of TGS1 or SMN deficiency on snRNA biogenesis and general transcription suggest that these proteins play interconnected roles in prevention of neurodegeneration.

Immature snRNA precursors produced by different snRNA genes differ in length (11,21,97–100). In human cells deficient for either TGS1 (this study) or TOE1 (3,96), the tails of the extended molecules generated by different U snRNA subclasses vary in length, number of templated nucleotides and number/type of untemplated residues. We found that in TGS1-deficient human cells and flies, the U2 snRNAs acquire different 3'-extended structures. While the majority of extended human U2 snRNAs have templated tails with or without an untemplated U residue, *Drosophila* U2 molecules preferentially gain untemplated uridines. Uridylation is thought to recognize misprocessed and/or low-quality snRNPs and target them for degradation (96,101–103). The variation in the 3' ends of snRNAs may reflect differences in promoter sequences (104), gene bodies or 3' regions, which are crucial determinants for the cleavage and maturation of the snRNA precursor transcripts (105). The different susceptibilities of individual snRNAs to loss of maturation factors might also depend on the specificity of these factors in 3'-end processing and on their residual levels. It is possible that TGS1 hypermethylates different snRNAs with different efficiencies and that our experimental conditions did not allow detection of differences in the hypermethylation level of U1 snRNA.

There is also evidence suggesting that the U1 snRNAs behave differently from the other U snRNA subclasses. Recent work has revealed that 3'-end processing of some snRNAs is a biphasic process that takes place both before and after the assembly with the SMN complex (96). Human U1 has a peculiar Sm core assembly pathway and differs from the other snRNAs in the affinity for SMN-Gemin5 (11,106). These features suggest a specific regulation of the biogenesis of the U1 snRNP, which is the most abundant snRNP, playing roles in both splicing and poly(A) site selection (telescripting) (107). Thus, the finding that the U1 snRNAs are not affected by loss of TGS1 might depend on several factors, including the specificity of the TGS1 enzymatic activity and the peculiar maturation pathway of the U1 snRNPs. We cannot rule out the possibility that in our hypomorphic mutants, a minimal residual TGS1 activity, that is sufficient to

sustain cell viability, is enough to provide the modification of U1 snRNA.

TGS1 deficiency results in extensive alterations in the human transcriptome, including changes in the efficiency of intron removal and accumulation of transcripts with 3' extensions spanning intergenic regions, and often incorporating exons of adjacent genes. Similar alterations are also observed in the transcriptome of *SMN* mutant cells. Long-read Oxford Nanopore Technology (ONT) sequencing confirmed that *TGS1*- and *SMN*-deficient cells accumulate mRNAs that carry both splicing and 3'-end cleavage defects. Many of these are chimeric transcripts, in which the exon of a gene is fused to exons of the downstream gene. Recent work has suggested that SMN directly mediates proper transcription termination by favoring Pol II release (108), and SMN deficiency has been linked to accumulation of R-loops and DNA damage (83,109). Accumulation of aberrant readthrough transcripts is consistent with these results and may contribute to the neurodegenerative defects observed in *TGS1* and *SMN* mutant models.

Previous work has shown that U2 snRNP alterations caused by deficiency of the SF3B1 protein result in splicing defects and transcription proceeding beyond the canonical polyadenylation [poly(A)] sites, leading to severe pathological consequences (61,110). In addition, it has been shown that U1 snRNPs prevent premature transcription termination before the last exon by inhibiting 3'-end cleavage at cryptic, early polyadenylation sites (107). The results of our long-read ONT sequencing of transcripts from *TGS1*- and *SMN*-deficient cells support the hypothesis that at least a fraction of the aberrant readthrough mRNAs observed in *TGS1* and *SMN* mutant cells are caused by a primary defect in splicing, and consolidate the notion that reduced efficiency of co-transcriptional splicing impairs correct transcription termination (111,112). However, given that the TMG cap contributes to nuclear import of snRNPs (16–20), it cannot be excluded that inefficient import of monomethylated snRNA precursors could decrease the levels of functional snRNPs, with possible repercussions on the efficiency of termination. Our observations are also compatible with the possibility that TGS1 cooperates with SMN in tran-



scription termination and that its loss directly contributes to the formation of long readthrough transcripts.

The characterization of transcriptional defects in *TGS1*- and *SMN*-deficient cells was carried out on steady-state poly(A) transcripts and therefore the occurrence of non-polyadenylated and unstable species that are subjected to clearance by the RNA surveillance machineries may have been overlooked. It has been reported that inverted Alu repeats promote the expression of circular RNAs from the *SMN* locus (113,114). In our sequencing datasets we did not find aberrant transcripts arising from the *SMN* loci; however, it is possible that transcriptional readthrough of the *SMN* gene might enhance the expression of *SMN* circular RNAs (113). Further analyses with methods that allow the isolation of non-polyadenylated transcripts as in (115) and (116) and by long-read sequencing of nascent RNA will probably expand the repertoire of RNAs affected by *TGS1* and *SMN* depletion.

Collectively, our data support a model where *TGS1* and *SMN* have closely related functions in preventing neurodegeneration (Figure 9A, B). *TGS1* plays roles in snRNA 3' maturation and its loss affects the accuracy of both pre-mRNA splicing and transcription termination. *SMN* promotes assembly of snRNA into snRNPs and is essential for splicing and efficient transcription termination (85,108). Thus, loss of either protein leads to substantial transcriptome alterations. These alterations may be neurotoxic by directly affecting specific transcripts important for neuronal survival and function, a scenario supported by increasing experimental evidence (92–94,117). In addition, reduced efficiency of splicing and transcription termination may be a source of transcriptional stress that results in genome-wide accumulation of R-loops and DNA damage, which may also affect neuronal survival (118). Future studies on ultra-fine characterization of aberrant mRNA molecules and their effects in neurons are needed to support this possibility, which has strong relevance not only for SMA but also for other neurodegenerative disorders. Importantly, we found that *TGS1* overexpression can partially rescue the neurological phenotypes caused by *SMN* depletion in the fly and worm models. Moreover, previous work has shown that *TGS1* directly interacts with the *SMN* protein in human cells (14), and that *Drosophila* *Tgs1* physically associates with most components of the *SMN* complex *in vivo* (40). Thus, the physical interaction between *TGS1* and *SMN* and the similar phenotypes elicited by their deficiency suggest a functional interaction between these proteins. We hypothesize that *TGS1* overexpression in *SMN*-depleted cells might enhance snRNP biogenesis and possibly improve the fidelity of splicing and transcription termination, functionally compensating at least in part for defects caused by *SMN* deficiency (Figure 9).

Recent remarkable advances in the field have led to the approval of disease-modifying therapies for SMA patients, which include *SMN* replacement via gene therapy as well as increased production of full-length *SMN* by splicing modulation with antisense oligonucleotides or small molecules (119–122). These treatments are most effective in improving the SMA phenotypes when administered to pre-symptomatic patients (123,124). However, an expansion of SMA therapeutic options that could comple-

ment *SMN*-inducing treatments is especially desirable for those patients displaying more limited clinical benefit due to delayed intervention or other variables (123). The development of *SMN*-independent strategies will require a more profound knowledge of disease-relevant downstream pathways (119,120,124–129). Studies in model organisms have led to the identification of factors, whose modulation can alter the pathogenic consequences of *SMN* deficiency (73,81,93,94,130). This study expands the list of these factors by showing that *TGS1* overexpression can compensate, at least in part, for *SMN* loss in animal models of neurodegeneration.

## DATA AVAILABILITY

The custom Python scripts used for the analysis of 3' RACE data are available at [https://github.com/cmroake/NAR\\_TGS1](https://github.com/cmroake/NAR_TGS1).

The custom R scripts used for the analysis of transcriptome data produced via Illumina sequencing are available at [https://github.com/roozbehdn/TGS1\\_SMN](https://github.com/roozbehdn/TGS1_SMN).

The RNAend-Seq data discussed in this publication have been deposited with links to BioProject accession number PRJNA628085 in the NCBI BioProject database (<https://www.ncbi.nlm.nih.gov/bioproject/>).

The Illumina and Nanopore RNA-Seq data discussed in this publication have been deposited in NCBI's Gene Expression Omnibus (131) and are accessible through GEO Series accession numbers GSE189413 and GSE189138, respectively.

## SUPPLEMENTARY DATA

Supplementary Data are available at NAR Online.

## ACKNOWLEDGEMENTS

We thank P. Bazzicalupo for critical reading of the manuscript, G. Zampi and F. Sola for technical support, S. Schneider for support in zebrafish procedures, and P. De Pianta for data analysis. For strains and plasmids, we thank A. Fire, K. Shen, O. Hobert, C. Bargmann and the Caenorhabditis Genetics Center (CGC), funded by the NIH Office of Research Infrastructure Programs (P40 OD010440). We thank Reinhard Lührmann for sharing the R1131 TMG antibody.

## FUNDING

This work was supported by grants from Telethon GPP13147 (to G.D.R.) and GGP16203 (to E.D.S.), NIH AG056575 and CA197563 (to S.E.A.), NS102451 (to L.P.), AIRC IG 20528 (to M.G.), AIRC IG 26496 (to G.D.R.), Italian Ministry of Economy and Finance (FaReBio di Qualità) and Italian Ministry of Health RF 2009-1473235 (to E.D.S.), German Research Foundation [Wi 945/17-1 (project-ID 398410809); FOR2722 (project ID 384170921); Wi 945/19-1 (project-ID 417989143); KY96.1-2 (project-ID 269018619); SFB1451 (project-ID 431549029 – A01), and GRK1960 (project ID 233886668)], the European Research Council (ERC)

under the European Union's Horizon 2020 research and innovation program under the Marie Skłodowska-Curie grant agreement No 956185 (SMABEYOND) and the Center for Molecular Medicine Cologne (project C18) (to B.W.). S.F. was supported by Fondazione Cariplo (grant 2014-1215) and by AriSLA (project DDRNA&ALS and DDR&ALS). A.C., G.P. and G.G.T are supported by European Research Council [RIBOMYLOME\_309545 and ASTRA\_855923] and the H2020 projects [IASIS\_727658 and INFORE\_825080]. L.C. was supported by a Stanford Cancer Institute 2018 Fellowship Award, and C.M.R. by an MSTP Training Grant GM007365 and a Gerald J. Lieberman Fellowship.

*Conflict of interest statement.* None declared.

## REFERENCES

- Nussbacher, J.K., Tabet, R., Yeo, G.W. and Lagier-Tourenne, C. (2019) Disruption of RNA metabolism in neurological diseases and emerging therapeutic interventions. *Neuron*, **102**, 294–320.
- Wirth, B., Karakaya, M., Kye, M.J. and Mendoza-Ferreira, N. (2020) Twenty-five years of spinal muscular atrophy research: from phenotype to genotype to therapy, and what comes next. *Annu. Rev. Genomics Hum. Genet.*, **21**, 231–261.
- Lardelli, R.M., Schaffer, A.E., Eggen, V.R., Zaki, M.S., Grainger, S., Sathe, S., Van Nostrand, E.L., Schlachetzki, Z., Rosti, B., Akizu, N. et al. (2017) Biallelic mutations in the 3' exonuclease TOE1 cause pontocerebellar hypoplasia and uncover a role in snRNA processing. *Nat. Genet.*, **49**, 457–464.
- de Vegvar, H.E., Lund, E. and Dahlberg, J.E. (1986) 3' end formation of U1 snRNA precursors is coupled to transcription from snRNA promoters. *Cell*, **47**, 259–266.
- Hernandez, N. and Weiner, A.M. (1986) Formation of the 3' end of U1 snRNA requires compatible snRNA promoter elements. *Cell*, **47**, 249–258.
- Egloff, S., Zaborowska, J., Laitem, C., Kiss, T. and Murphy, S. (2012) Ser7 phosphorylation of the CTD recruits the RPA2 ser5 phosphatase to snRNA genes. *Mol. Cell*, **45**, 111–122.
- O'Reilly, D., Kuznetsova, O.V., Laitem, C., Zaborowska, J., Dienstbier, M. and Murphy, S. (2014) Human snRNA genes use polyadenylation factors to promote efficient transcription termination. *Nucleic Acids Res.*, **42**, 264–275.
- Baillat, D., Hakimi, M.A., Naar, A.M., Shilatfard, A., Cooch, N. and Shiekhattar, R. (2005) Integrator, a multiprotein mediator of small nuclear RNA processing, associates with the C-terminal repeat of RNA polymerase II. *Cell*, **123**, 265–276.
- Ohno, M., Segref, A., Bachi, A., Wilm, M. and Mattaj, I.W. (2000) PHAX, a mediator of U snRNA nuclear export whose activity is regulated by phosphorylation. *Cell*, **101**, 187–198.
- Kitao, S., Segref, A., Kast, J., Wilm, M., Mattaj, I.W. and Ohno, M. (2008) A compartmentalized phosphorylation/dephosphorylation system that regulates U snRNA export from the nucleus. *Mol. Cell Biol.*, **28**, 487–497.
- Yong, J., Kasim, M., Bachorik, J.L., Wan, L. and Dreyfuss, G. (2010) Gemin5 delivers snRNA precursors to the SMN complex for snRNP biogenesis. *Mol. Cell*, **38**, 551–562.
- Pellizzoni, L., Yong, J. and Dreyfuss, G. (2002) Essential role for the SMN complex in the specificity of snRNP assembly. *Science*, **298**, 1775–1779.
- Mouaikel, J., Verheggen, C., Bertrand, E., Tazi, J. and Bordonne, R. (2002) Hypermethylation of the cap structure of both yeast snRNAs and snoRNAs requires a conserved methyltransferase that is localized to the nucleolus. *Mol. Cell*, **9**, 891–901.
- Mouaikel, J., Narayanan, U., Verheggen, C., Matera, A.G., Bertrand, E., Tazi, J. and Bordonne, R. (2003) Interaction between the small-nuclear-RNA cap methylase and the spinal muscular atrophy protein, survival of motor neuron. *EMBO Rep.*, **4**, 616–622.
- Narayanan, U., Achsel, T., Luhrmann, R. and Matera, A.G. (2004) Coupled in vitro import of U snRNPs and SMN, the spinal muscular atrophy protein. *Mol. Cell*, **16**, 223–234.
- Strasser, A., Dickmanns, A., Luhrmann, R. and Ficner, R. (2005) Structural basis for m3G-cap-mediated nuclear import of spliceosomal snRNPs by snurportin1. *EMBO J.*, **24**, 2235–2243.
- Fischer, U., Heinrich, J., van Zee, K., Fanning, E. and Luhrmann, R. (1994) Nuclear transport of U1 snRNP in somatic cells: differences in signal requirement compared with *Xenopus laevis* oocytes. *J. Cell Biol.*, **125**, 971–980.
- Marshall, C. and Luhrmann, R. (1994) In vitro nuclear import of snRNPs: cytosolic factors mediate m3G-cap dependence of U1 and U2 snRNP transport. *EMBO J.*, **13**, 222–231.
- Huber, J., Cronshagen, U., Kadokura, M., Marshall, C., Wada, T., Sekine, M. and Luhrmann, R. (1998) Snurportin1, an m3G-cap-specific nuclear import receptor with a novel domain structure. *EMBO J.*, **17**, 4114–4126.
- Stanek, D. (2017) Cajal bodies and snRNPs—friends with benefits. *RNA Biol.*, **14**, 671–679.
- Wieben, E.D., Nenner, J.M. and Pederson, T. (1985) Ribonucleoprotein organization of eukaryotic RNA. XXXII. U2 small nuclear RNA precursors and their accurate 3' processing in vitro as ribonucleoprotein particles. *J. Mol. Biol.*, **183**, 69–78.
- Brenner, S. (1974) The genetics of *Caenorhabditis elegans*. *Genetics*, **77**, 71–94.
- Gallotta, I., Mazzarella, N., Donato, A., Esposito, A., Chaplin, J.C., Castro, S., Zampi, G., Battaglia, G.S., Hilliard, M.A., Bazzicalupo, P. et al. (2016) Neuron-specific knock-down of SMN1 causes neuron degeneration and death through an apoptotic mechanism. *Hum. Mol. Genet.*, **25**, 2564–2577.
- Hobert, O. (2002) PCR fusion-based approach to create reporter gene constructs for expression analysis in transgenic *C. elegans*. *BioTechniques*, **32**, 728–730.
- Esposito, G., Di Schiavi, E., Bergamasco, C. and Bazzicalupo, P. (2007) Efficient and cell specific knock-down of gene function in targeted *C. elegans* neurons. *Gene*, **395**, 170–176.
- Eastman, C., Horvitz, H.R. and Jin, Y. (1999) Coordinated transcriptional regulation of the unc-25 glutamic acid decarboxylase and the unc-47 GABA vesicular transporter by the *Caenorhabditis elegans* UNC-30 homeodomain protein. *J. Neurosci.*, **19**, 6225–6234.
- Kamath, R.S., Fraser, A.G., Dong, Y., Poulin, G., Durbin, R., Gotta, M., Kanapin, A., Le Bot, N., Moreno, S., Sohrmann, M. et al. (2003) Systematic functional analysis of the *Caenorhabditis elegans* genome using RNAi. *Nature*, **421**, 231–237.
- Mello, C.C., Kramer, J.M., Stinchcomb, D. and Ambros, V. (1991) Efficient gene transfer in *C. elegans*: extrachromosomal maintenance and integration of transforming sequences. *EMBO J.*, **10**, 3959–3970.
- Veronico, P., Gray, L.J., Jones, J.T., Bazzicalupo, P., Arbucci, S., Cortese, M.R., Di Vito, M. and De Giorgi, C. (2001) Nematode chitin synthases: gene structure, expression and function in *Caenorhabditis elegans* and the plant parasitic nematode *Meloidogyne artiellia*. *Mol. Genet. Genomics*, **266**, 28–34.
- Kimble, J.E. and White, J.G. (1981) On the control of germ cell development in *Caenorhabditis elegans*. *Dev. Biol.*, **81**, 208–219.
- Stinchcomb, D.T., Shaw, J.E., Carr, S.H. and Hirsh, D. (1985) Extrachromosomal DNA transformation of *Caenorhabditis elegans*. *Mol. Cell Biol.*, **5**, 3484–3496.
- McIntire, S.L., Reimer, R.J., Schuske, K., Edwards, R.H. and Jorgensen, E.M. (1997) Identification and characterization of the vesicular GABA transporter. *Nature*, **389**, 870–876.
- Riessland, M., Kaczmarek, A., Schneider, S., Swoboda, K.J., Lohr, H., Bradler, C., Grysko, V., Dimitriadi, M., Hosseinbarkoobe, S., Torres-Benito, L. et al. (2017) Neurocalcin delta suppression protects against spinal muscular atrophy in humans and across species by restoring impaired endocytosis. *Am. J. Hum. Genet.*, **100**, 297–315.
- Mendoza-Ferreira, N., Coutelier, M., Janzen, E., Hosseinbarkoobe, S., Lohr, H., Schneider, S., Milbradt, J., Karakaya, M., Riessland, M., Pichlo, C. et al. (2018) Biallelic CHP1 mutation causes human autosomal recessive ataxia by impairing NHE1 function. *Neurol. Genet.*, **4**, e209.
- Lan, C.C., Tang, R., Un San Leong, I. and Love, D.R. (2009) Quantitative real-time RT-PCR (qRT-PCR) of zebrafish transcripts: optimization of RNA extraction, quality control considerations, and data analysis. *Cold Spring Harb. Protoc.*, **2009**, pdb prot5314.
- Oprea, G.E., Krober, S., McWhorter, M.L., Rossoll, W., Muller, S., Krawczak, M., Bassell, G.J., Beattie, C.E. and Wirth, B. (2008) Platin

- 3 is a protective modifier of autosomal recessive spinal muscular atrophy. *Science*, **320**, 524–527.
37. Chang, H.C., Dimlich, D.N., Yokokura, T., Mukherjee, A., Kankel, M.W., Sen, A., Sridhar, V., Fulga, T.A., Hart, A.C., Van Vactor, D. *et al.* (2008) Modeling spinal muscular atrophy in *Drosophila*. *PLoS One*, **3**, e3209.
  38. Palumbo, V., Pellacani, C., Heesom, K.J., Rogala, K.B., Deane, C.M., Mottier-Pavie, V., Gatti, M., Bonaccorsi, S. and Wakefield, J.G. (2015) Misato controls mitotic microtubule generation by stabilizing the TCP-1 tubulin chaperone complex [corrected]. *Curr. Biol.*, **25**, 1777–1783.
  39. Bischof, J., Maeda, R.K., Hediger, M., Karch, F. and Basler, K. (2007) An optimized transgenesis system for *Drosophila* using germ-line-specific phiC31 integrases. *Proc. Natl Acad. Sci. USA*, **104**, 3312–3317.
  40. Maccallini, P., Bavasso, F., Scatolini, L., Bucciarelli, E., Noviello, G., Lisi, V., Palumbo, V., D'Angeli, S., Cacchione, S., Cenci, G. *et al.* (2020) Intimate functional interactions between TGS1 and the SMN complex revealed by an analysis of the *Drosophila* eye development. *PLoS Genet.*, **16**, e1008815.
  41. Buszczak, M., Paterno, S., Lighthouse, D., Bachman, J., Planck, J., Owen, S., Skora, A.D., Nystul, T.G., Ohlstein, B., Allen, A. *et al.* (2007) The Carnegie protein trap library: a versatile tool for *Drosophila* developmental studies. *Genetics*, **175**, 1505–1531.
  42. Raffa, G.D., Siriaco, G., Cugusi, S., Ciapponi, L., Cenci, G., Wojcik, E. and Gatti, M. (2009) The *Drosophila* modigliani (moi) gene encodes a HOAP-interacting protein required for telomere protection. *Proc. Natl Acad. Sci. USA*, **106**, 2271–2276.
  43. Lattao, R., Bonaccorsi, S., Guan, X., Wasserman, S.A. and Gatti, M. (2011) Tubby-tagged balancers for the *Drosophila* X and second chromosomes. *Fly*, **5**, 369–370.
  44. Ran, F.A., Hsu, P.D., Wright, J., Agarwala, V., Scott, D.A. and Zhang, F. (2013) Genome engineering using the CRISPR-Cas9 system. *Nat. Protoc.*, **8**, 2281–2308.
  45. Chen, L., Roake, C.M., Galati, A., Bavasso, F., Micheli, E., Saggio, I., Schoefer, S., Cacchione, S., Gatti, M., Artandi, S.E. *et al.* (2020) Loss of human TGS1 hypermethylase promotes increased telomerase RNA and telomere elongation. *Cell Rep.*, **30**, 1358–1372.
  46. Xu, L. and Blackburn, E.H. (2007) Human cancer cells harbor T-stumps, a distinct class of extremely short telomeres. *Mol. Cell*, **28**, 315–327.
  47. Roake, C.M., Chen, L., Chakravarthy, A.L., Ferrell, J.E., Raffa, G.D. and Artandi, S.E. (2019) Disruption of telomerase RNA maturation kinetics precipitates disease. *Mol. Cell*, **74**, 688–700.
  48. Chen, L., Roake, C.M., Freund, A., Batista, P.J., Tian, S., Yin, Y.A., Gajera, C.R., Lin, S., Lee, B., Pech, M.F. *et al.* (2018) An activity switch in human telomerase based on RNA conformation and shaped by TCAB1. *Cell*, **174**, 218–230.
  49. Venteicher, A.S., Abreu, E.B., Meng, Z., McCann, K.E., Terns, R.M., Veenstra, T.D., Terns, M.P. and Artandi, S.E. (2009) A human telomerase holoenzyme protein required for cajal body localization and telomere synthesis. *Science*, **323**, 644–648.
  50. Luhrmann, R., Appel, B., Bringmann, P., Rinke, J., Reuter, R., Rothe, S. and Bald, R. (1982) Isolation and characterization of rabbit anti-m3 2,2,7G antibodies. *Nucleic Acids Res.*, **10**, 7103–7113.
  51. Petrov, A., Wu, T., Puglisi, E.V. and Puglisi, J.D. (2013) RNA purification by preparative polyacrylamide gel electrophoresis. *Methods Enzymol.*, **530**, 315–330.
  52. Livak, K.J. and Schmittgen, T.D. (2001) Analysis of relative gene expression data using real-time quantitative PCR and the 2(-Delta delta C(T)) method. *Methods*, **25**, 402–408.
  53. Chen, L., Ooi, S.K., Conaway, R.C. and Conaway, J.W. (2014) Generation and purification of human INO80 chromatin remodeling complexes and subcomplexes. *J. Vis. Exp.*, e51720.
  54. Wu, Y., Xu, W., Ma, L., Yu, Z., Wang, Y. and Yu, C.R. (2022) Robust and sensitive in situ RNA detection using Yn-situ. *Cell Rep. Methods*, **2**, 100201.
  55. Dobin, A., Davis, C.A., Schlesinger, F., Drenkow, J., Zaleski, C., Jha, S., Batut, P., Chaisson, M. and Gingeras, T.R. (2013) STAR: ultrafast universal RNA-seq aligner. *Bioinformatics*, **29**, 15–21.
  56. Shao, M. and Kingsford, C. (2017) Accurate assembly of transcripts through phase-preserving graph decomposition. *Nat. Biotechnol.*, **35**, 1167–1169.
  57. Pimentel, H., Bray, N.L., Puente, S., Melsted, P. and Pachter, L. (2017) Differential analysis of RNA-seq incorporating quantification uncertainty. *Nat. Methods*, **14**, 687–690.
  58. Trincado, J.L., Entizne, J.C., Hysenaj, G., Singh, B., Skalic, M., Elliott, D.J. and Eyras, E. (2018) SUPPA2: fast, accurate, and uncertainty-aware differential splicing analysis across multiple conditions. *Genome Biol.*, **19**, 40.
  59. Patro, R., Duggal, G., Love, M.I., Irizarry, R.A. and Kingsford, C. (2017) Salmon provides fast and bias-aware quantification of transcript expression. *Nat. Methods*, **14**, 417–419.
  60. Li, H. (2018) Minimap2: pairwise alignment for nucleotide sequences. *Bioinformatics*, **34**, 3094–3100.
  61. Tang, A.D., Soulette, C.M., van Baren, M.J., Hart, K., Hrabeta-Robinson, E., Wu, C.J. and Brooks, A.N. (2020) Full-length transcript characterization of SF3B1 mutation in chronic lymphocytic leukemia reveals downregulation of retained introns. *Nat. Commun.*, **11**, 1438.
  62. Frankish, A., Diekhans, M., Ferreira, A.M., Johnson, R., Jungreis, I., Loveland, J., Mudge, J.M., Sisu, C., Wright, J., Armstrong, J. *et al.* (2019) GENCODE reference annotation for the human and mouse genomes. *Nucleic Acids Res.*, **47**, D766–D773.
  63. Quinlan, A.R. and Hall, I.M. (2010) BEDTools: a flexible suite of utilities for comparing genomic features. *Bioinformatics*, **26**, 841–842.
  64. Shaye, D.D. and Greenwald, I. (2011) OrthoList: a compendium of *C. elegans* genes with human orthologs. *PLoS One*, **6**, e20085.
  65. Spencer, W.C., Zeller, G., Watson, J.D., Henz, S.R., Watkins, K.L., McWhirter, R.D., Petersen, S., Sreedharan, V.T., Widmer, C., Jo, J. *et al.* (2011) A spatial and temporal map of *C. elegans* gene expression. *Genome Res.*, **21**, 325–341.
  66. Kaletsky, R., Lakhina, V., Arey, R., Williams, A., Landis, J., Ashraf, J. and Murphy, C.T. (2016) The *C. elegans* adult neuronal IIS/FOXO transcriptome reveals adult phenotype regulators. *Nature*, **529**, 92–96.
  67. Rugarli, E.I., Di Schiavi, E., Hilliard, M.A., Arbucci, S., Ghezzi, C., Faccioli, A., Coppola, G., Ballabio, A. and Bazzicalupo, P. (2002) The kallmann syndrome gene homolog in *C. elegans* is involved in epidermal morphogenesis and neurite branching. *Development*, **129**, 1283–1294.
  68. McIntire, S.L., Jorgensen, E., Kaplan, J. and Horvitz, H.R. (1993) The GABAergic nervous system of *Caenorhabditis elegans*. *Nature*, **364**, 337–341.
  69. Komonyi, O., Schauer, T., Papai, G., Deak, P. and Boros, I.M. (2009) A product of the bicistronic *Drosophila melanogaster* gene CG31241, which also encodes a trimethylguanosine synthase, plays a role in telomere protection. *J. Cell Sci.*, **122**, 769–774.
  70. Borg, R.M., Fenech Salerno, B., Vassallo, N., Bordonne, R. and Cauchi, R.J. (2016) Disruption of snRNP biogenesis factors tgs1 and piCln induces phenotypes that mirror aspects of SMN-Gemins complex perturbation in *Drosophila*, providing new insights into spinal muscular atrophy. *Neurobiol. Dis.*, **94**, 245–258.
  71. Di Giorgio, M.L., Esposito, A., Maccallini, P., Micheli, E., Bavasso, F., Gallotta, I., Verni, F., Feiguin, F., Cacchione, S., McCabe, B.D. *et al.* (2017) WDR79/TCAB1 plays a conserved role in the control of locomotion and ameliorates phenotypic defects in SMA models. *Neurobiol. Dis.*, **105**, 42–50.
  72. McWhorter, M.L., Monani, U.R., Burghes, A.H. and Beattie, C.E. (2003) Knockdown of the survival motor neuron (Smn) protein in zebrafish causes defects in motor axon outgrowth and pathfinding. *J. Cell Biol.*, **162**, 919–931.
  73. Hosseinibarkoobe, S., Peters, M., Torres-Benito, L., Rastetter, R.H., Hupperich, K., Hoffmann, A., Mendoza-Ferreira, N., Kaczmarek, A., Janzen, E., Milbradt, J. *et al.* (2016) The power of human protective modifiers: PLS3 and CORO1C unravel impaired endocytosis in spinal muscular atrophy and rescue SMA phenotype. *Am. J. Hum. Genet.*, **99**, 647–665.
  74. Tisdale, S. and Pellizzoni, L. (2015) Disease mechanisms and therapeutic approaches in spinal muscular atrophy. *J. Neurosci.*, **35**, 8691–8700.
  75. Lemm, I., Girard, C., Kuhn, A.N., Watkins, N.J., Schneider, M., Bordonne, R. and Luhrmann, R. (2006) Ongoing U snRNP biogenesis is required for the integrity of Cajal bodies. *Mol. Biol. Cell*, **17**, 3221–3231.



76. Tycowski, K.T., Aab, A. and Steitz, J.A. (2004) Guide RNAs with 5' caps and novel box C/D snoRNA-like domains for modification of snRNAs in metazoa. *Curr. Biol.*, **14**, 1985–1995.
77. Jia, D., Cai, L., He, H., Skogerbo, G., Li, T., Aftab, M.N. and Chen, R. (2007) Systematic identification of non-coding RNA 2,2,7-trimethylguanosine cap structures in *Caenorhabditis elegans*. *BMC Mol. Biol.*, **8**, 86.
78. Becker, D., Hirsch, A.G., Bender, L., Lingner, T., Salinas, G. and Krebber, H. (2019) Nuclear pre-snRNA export is an essential quality assurance mechanism for functional spliceosomes. *Cell Rep.*, **27**, 3199–3214.
79. Goldfarb, K.C. and Cech, T.R. (2013) 3' terminal diversity of MRP RNA and other human noncoding RNAs revealed by deep sequencing. *BMC Mol. Biol.*, **14**, 23.
80. Cho, H.D., Tomita, K., Suzuki, T. and Weiner, A.M. (2002) U2 small nuclear RNA is a substrate for the CCA-adding enzyme (tRNA nucleotidyltransferase). *J. Biol. Chem.*, **277**, 3447–3455.
81. Rizzo, F., Nizzardo, M., Vashisht, S., Molteni, E., Melzi, V., Taiana, M., Salani, S., Santonicola, P., Di Schiavi, E., Bucchia, M. et al. (2019) Key role of SMN/SYNERG1 and RNA-Motif 7 in spinal muscular atrophy: RNA-Seq and motif analysis of human motor neurons. *Brain*, **142**, 276–294.
82. Doktor, T.K., Hua, Y., Andersen, H.S., Broner, S., Liu, Y.H., Wieckowska, A., Dembic, M., Bruun, G.H., Krainer, A.R. and Andresen, B.S. (2017) RNA-sequencing of a mouse-model of spinal muscular atrophy reveals tissue-wide changes in splicing of U12-dependent introns. *Nucleic Acids Res.*, **45**, 395–416.
83. Jangi, M., Fleet, C., Cullen, P., Gupta, S.V., Mekhoubad, S., Chiao, E., Allaire, N., Bennett, C.F., Rigo, F., Krainer, A.R. et al. (2017) SMN deficiency in severe models of spinal muscular atrophy causes widespread intron retention and DNA damage. *Proc. Natl Acad. Sci. USA*, **114**, E2347–E2356.
84. Huo, Q., Kayikci, M., Odermatt, P., Meyer, K., Michels, O., Saxena, S., Ule, J. and Schumperli, D. (2014) Splicing changes in SMA mouse motoneurons and SMN-depleted neuroblastoma cells: evidence for involvement of splicing regulatory proteins. *RNA Biol.*, **11**, 1430–1446.
85. Zhang, Z., Lotti, F., Dittmar, K., Younis, I., Wan, L., Kasim, M. and Dreyfuss, G. (2008) SMN deficiency causes tissue-specific perturbations in the repertoire of snRNAs and widespread defects in splicing. *Cell*, **133**, 585–600.
86. Lotti, F., Imlach, W.L., Saieva, L., Beck, E.S., Hao, L.T., Li, D.K., Jiao, W., Mentis, G.Z., Beattie, C.E., McCabe, B.D. et al. (2012) An SMN-dependent U12 splicing event essential for motor circuit function. *Cell*, **151**, 440–454.
87. Bray, N.L., Pimentel, H., Melsted, P. and Pachter, L. (2016) Near-optimal probabilistic RNA-seq quantification. *Nat. Biotechnol.*, **34**, 525–527.
88. Peabody, N.C., Dia, F., Luan, H., Wang, H., Dewey, E.M., Honninger, H.W. and White, B.H. (2008) Bursicon functions within the *Drosophila* CNS to modulate wing expansion behavior, hormone secretion, and cell death. *J. Neurosci.*, **28**, 14379–14391.
89. Jia, Y., Mu, J.C. and Ackerman, S.L. (2012) Mutation of a U2 snRNA gene causes global disruption of alternative splicing and neurodegeneration. *Cell*, **148**, 296–308.
90. Tisdale, S., Lotti, F., Saieva, L., Van Meerbeke, J.P., Crawford, T.O., Sumner, C.J., Mentis, G.Z. and Pellizzoni, L. (2013) SMN is essential for the biogenesis of U7 small nuclear ribonucleoprotein and 3'-end formation of histone mRNAs. *Cell Rep.*, **5**, 1187–1195.
91. Ruggiu, M., McGovern, V.L., Lotti, F., Saieva, L., Li, D.K., Kariya, S., Monani, U.R., Burghes, A.H. and Pellizzoni, L. (2012) A role for SMN exon 7 splicing in the selective vulnerability of motor neurons in spinal muscular atrophy. *Mol. Cell Biol.*, **32**, 126–138.
92. Simon, C.M., Dai, Y., Van Alstyne, M., Koutsidoumpa, C., Pagiazitis, J.G., Chalif, J.I., Wang, X., Rabinowitz, J.E., Henderson, C.E., Pellizzoni, L. et al. (2017) Converging mechanisms of p53 activation drive motor neuron degeneration in spinal muscular atrophy. *Cell Rep.*, **21**, 3767–3780.
93. Simon, C.M., Van Alstyne, M., Lotti, F., Bianchetti, E., Tisdale, S., Watterson, D.M., Mentis, G.Z. and Pellizzoni, L. (2019) Stasimon contributes to the loss of sensory synapses and motor neuron death in a mouse model of spinal muscular atrophy. *Cell Rep.*, **29**, 3885–3901.
94. Van Alstyne, M., Simon, C.M., Sardi, S.P., Shihabuddin, L.S., Mentis, G.Z. and Pellizzoni, L. (2018) Dysregulation of mdm2 and mdm4 alternative splicing underlies motor neuron death in spinal muscular atrophy. *Genes Dev.*, **32**, 1045–1059.
95. Son, A., Park, J.E. and Kim, V.N. (2018) PARN and TOE1 constitute a 3' end maturation module for nuclear non-coding RNAs. *Cell Rep.*, **23**, 888–898.
96. Lardelli, R.M. and Lykke-Andersen, J. (2020) Competition between maturation and degradation drives human snRNA 3' end quality control. *Genes Dev.*, **34**, 989–1001.
97. Cheng, L., Zhang, Y., Zhang, Y., Chen, T., Xu, Y.Z. and Rong, Y.S. (2020) Loss of the RNA trimethylguanosine cap is compatible with nuclear accumulation of spliceosomal snRNAs but not pre-mRNA splicing or snRNA processing during animal development. *PLoS Genet.*, **16**, e1009098.
98. Madore, S.J., Wieben, E.D., Kunkel, G.R. and Pederson, T. (1984) Precursors of U4 small nuclear RNA. *J. Cell Biol.*, **99**, 1140–1144.
99. Madore, S.J., Wieben, E.D. and Pederson, T. (1984) Intracellular site of U1 small nuclear RNA processing and ribonucleoprotein assembly. *J. Cell Biol.*, **98**, 188–192.
100. Ezzeddine, N., Chen, J., Waltenspiel, B., Burch, B., Albrecht, T., Zhuo, M., Warren, W.D., Marzluff, W.F. and Wagner, E.J. (2011) A subset of *Drosophila* integrator proteins is essential for efficient U7 snRNA and spliceosomal snRNA 3'-end formation. *Mol. Cell Biol.*, **31**, 328–341.
101. Shukla, S. and Parker, R. (2014) Quality control of assembly-defective U1 snRNAs by decapping and 5'-to-3' exonucleolytic digestion. *Proc. Natl Acad. Sci. USA*, **111**, E3277–E3286.
102. Roithova, A., Feketova, Z., Vanacova, S. and Stanek, D. (2020) DIS3L2 and LSM proteins are involved in the surveillance of sm ring-deficient snRNAs. *Nucleic Acids Res.*, **48**, 6184–6197.
103. Reimao-Pinto, M.M., Manzenreither, R.A., Burkard, T.R., Sledz, P., Jinek, M., Mechtler, K. and Ameres, S.L. (2016) Molecular basis for cytoplasmic RNA surveillance by uridylation-triggered decay in *Drosophila*. *EMBO J.*, **35**, 2417–2434.
104. Ramamurthy, L., Ingledue, T.C., Pilch, D.R., Kay, B.K. and Marzluff, W.F. (1996) Increasing the distance between the snRNA promoter and the 3' box decreases the efficiency of snRNA 3'-end formation. *Nucleic Acids Res.*, **24**, 4525–4534.
105. Guiro, J. and Murphy, S. (2017) Regulation of expression of human RNA polymerase II-transcribed snRNA genes. *Open Biol.*, **7**, 170073.
106. So, B.R., Wan, L., Zhang, Z., Li, P., Babiash, E., Duan, J., Younis, I. and Dreyfuss, G. (2016) A U1 snRNP-specific assembly pathway reveals the SMN complex as a versatile hub for RNP exchange. *Nat. Struct. Mol. Biol.*, **23**, 225–230.
107. Venters, C.C., Oh, J.M., Di, C., So, B.R. and Dreyfuss, G. (2019) U1 snRNP telescripting: suppression of premature transcription termination in introns as a new layer of gene regulation. *Cold Spring Harb. Perspect. Biol.*, **11**, a032235.
108. Zhao, D.Y., Gish, G., Braunschweig, U., Li, Y., Ni, Z., Schmitges, F.W., Zhong, G., Liu, K., Li, W., Moffat, J. et al. (2016) SMN and symmetric arginine dimethylation of RNA polymerase II C-terminal domain control termination. *Nature*, **529**, 48–53.
109. Kannan, A., Bhatia, K., Branzei, D. and Gangwani, L. (2018) Combined deficiency of senataxin and DNA-PKcs causes DNA damage accumulation and neurodegeneration in spinal muscular atrophy. *Nucleic Acids Res.*, **46**, 8326–8346.
110. Reimer, K.A., Mimoso, C.A., Adelman, K. and Neugebauer, K.M. (2021) Co-transcriptional splicing regulates 3' end cleavage during mammalian erythropoiesis. *Mol. Cell*, **81**, 998–101.
111. Rosa-Mercado, N.A., Zimmer, J.T., Apostolidi, M., Rinehart, J., Simon, M.D. and Steitz, J.A. (2021) Hyperosmotic stress alters the RNA polymerase II interactome and induces readthrough transcription despite widespread transcriptional repression. *Mol. Cell*, **81**, 502–513.
112. Alpert, T., Straube, K., Carrillo Oesterreich, F., Herzel, L. and Neugebauer, K.M. (2020) Widespread transcriptional readthrough caused by nab2 depletion leads to chimeric transcripts with retained introns. *Cell Rep.*, **33**, 108324.
113. Ottesen, E.W., Luo, D., Seo, J., Singh, N.N. and Singh, R.N. (2019) Human survival motor neuron genes generate a vast repertoire of circular RNAs. *Nucleic Acids Res.*, **47**, 2884–2905.

114. Pagliarini, V., Jolly, A., Bielli, P., Di Rosa, V., De la Grange, P. and Sette, C. (2020) Sam68 binds Alu-rich introns in SMN and promotes pre-mRNA circularization. *Nucleic Acids Res.*, **48**, 633–645.
115. Arnold, M., Bressin, A., Jasnovidova, O., Meierhofer, D. and Mayer, A. (2021) A BRD4-mediated elongation control point primes transcribing RNA polymerase II for 3'-processing and termination. *Mol. Cell*, **81**, 3589–3603.
116. Drexler, H.L., Choquet, K., Merens, H.E., Tang, P.S., Simpson, J.T. and Churchman, L.S. (2021) Revealing nascent RNA processing dynamics with nano-COP. *Nat. Protoc.*, **16**, 1343–1375.
117. Osman, E.Y., Van Alstyne, M., Yen, P.F., Lotti, F., Feng, Z., Ling, K.K., Ko, C.P., Pellizzoni, L. and Lorson, C.L. (2020) Minor snRNA gene delivery improves the loss of proprioceptive synapses on SMA motor neurons. *JCI Insight*, **5**, e130574.
118. Kannan, A., Jiang, X., He, L., Ahmad, S. and Gangwani, L. (2020) ZPR1 prevents R-loop accumulation, upregulates SMN2 expression and rescues spinal muscular atrophy. *Brain*, **143**, 69–93.
119. Mendell, J.R., Al-Zaidy, S., Shell, R., Arnold, W.D., Rodino-Klapac, L.R., Prior, T.W., Lowes, L., Alfano, L., Berry, K., Church, K. *et al.* (2017) Single-dose gene-replacement therapy for spinal muscular atrophy. *N. Engl. J. Med.*, **377**, 1713–1722.
120. Finkel, R.S., Chiriboga, C.A., Vajsar, J., Day, J.W., Montes, J., De Vivo, D.C., Yamashita, M., Rigo, F., Hung, G., Schneider, E. *et al.* (2016) Treatment of infantile-onset spinal muscular atrophy with nusinersen: a phase 2, open-label, dose-escalation study. *Lancet*, **388**, 3017–3026.
121. Darras, B.T., Masson, R., Mazurkiewicz-Beldzinska, M., Rose, K., Xiong, H., Zanuteli, E., Baranello, G., Bruno, C., Vlodayets, D., Wang, Y. *et al.* (2021) Risdiplam-treated infants with type 1 spinal muscular atrophy versus historical controls. *N. Engl. J. Med.*, **385**, 427–435.
122. Baranello, G., Darras, B.T., Day, J.W., Deconinck, N., Klein, A., Masson, R., Mercuri, E., Rose, K., El-Khairi, M., Gerber, M. *et al.* (2021) Risdiplam in type 1 spinal muscular atrophy. *N. Engl. J. Med.*, **384**, 915–923.
123. Chaytow, H., Faller, K.M.E., Huang, Y.T. and Gillingwater, T.H. (2021) Spinal muscular atrophy: from approved therapies to future therapeutic targets for personalized medicine. *Cell Rep. Med.*, **2**, 100346.
124. Blatnik, A.J. 3rd, McGovern, V.L. and Burghes, A.H.M. (2021) What genetics has told us and how it can inform future experiments for spinal muscular atrophy, a perspective. *Int. J. Mol. Sci.*, **22**, 8494.
125. Hosseinibarkooie, S., Schneider, S. and Wirth, B. (2017) Advances in understanding the role of disease-associated proteins in spinal muscular atrophy. *Expert Rev. Proteomics*, **14**, 581–592.
126. Sumner, C.J. and Crawford, T.O. (2018) Two breakthrough gene-targeted treatments for spinal muscular atrophy: challenges remain. *J. Clin. Invest.*, **128**, 3219–3227.
127. Talbot, K. and Tizzano, E.F. (2017) The clinical landscape for SMA in a new therapeutic era. *Gene Ther.*, **24**, 529–533.
128. Costa-Roger, M., Blasco-Perez, L., Cusco, I. and Tizzano, E.F. (2021) The importance of digging into the genetics of SMN genes in the therapeutic scenario of spinal muscular atrophy. *Int. J. Mol. Sci.*, **22**, 9029.
129. Wirth, B. (2021) Spinal muscular atrophy: in the challenge lies a solution. *Trends Neurosci.*, **44**, 306–322.
130. Janzen, E., Mendoza-Ferreira, N., Hosseinibarkooie, S., Schneider, S., Hupperich, K., Tschanz, T., Grysko, V., Riessland, M., Hammerschmidt, M., Rigo, F. *et al.* (2018) CHP1 reduction ameliorates spinal muscular atrophy pathology by restoring calcineurin activity and endocytosis. *Brain*, **141**, 2343–2361.
131. Edgar, R., Domrachev, M. and Lash, A.E. (2002) Gene expression omnibus: NCBI gene expression and hybridization array data repository. *Nucleic Acids Res.*, **30**, 207–210.